Platinum transport in chloride-bearing fluids and melts: Insights from in situ X-ray absorption spectroscopy and thermodynamic modeling

Tagirov, B. R.; Filimonova, O.; Trigub, A. L.; Akinfiev, N. N.; Nickolsky, M. S.; Kvashnina, K. O.; Chareev, D. A.; Zotov, A. V.;

Originally published:

March 2019

Geochimica et Cosmochimica Acta 254(2019), 86-101

DOI: https://doi.org/10.1016/j.gca.2019.03.023

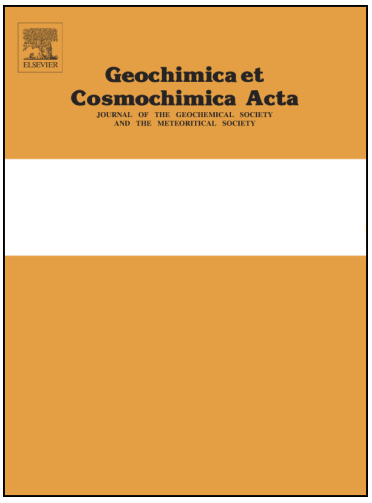

Platinum transport in chloride-bearing fluids and melts: insights from in situ X-ray absorption spectroscopy and thermodynamic modeling

Boris R. Tagirov, Olga N. Filimonova, Alexander L. Trigub, Nikolay N. Akinfiev, Maximilian S. Nickolsky, Kristina O. Kvashnina, Dmitriy A. Chareev, Alexander V. Zotov

PII: S0016-7037(19)30181-4
DOI: https://doi.org/10.1016/j.gca.2019.03.023
Reference: GCA 11179

To appear in: *Geochimica et Cosmochimica Acta*

Received Date: 2 October 2018
Accepted Date: 19 March 2019

Please cite this article as: Tagirov, B.R., Filimonova, O.N., Trigub, A.L., Akinfiev, N.N., Nickolsky, M.S., Kvashnina, K.O., Chareev, D.A., Zotov, A.V., Platinum transport in chloride-bearing fluids and melts: insights from in situ X-ray absorption spectroscopy and thermodynamic modeling, *Geochimica et Cosmochimica Acta* (2019), doi: https://doi.org/10.1016/j.gca.2019.03.023

Platinum transport in chloride-bearing fluids and melts: insights from in situ X-ray absorption spectroscopy and thermodynamic modeling

Boris R. Tagirov[1]*, Olga N. Filimonova[1], Alexander L. Trigub[2,1], Nikolay N. Akinfiev[1,6], Maximilian S. Nickolsky[1], Kristina O. Kvashnina[3,4], Dmitriy A. Chareev[5,1], Alexander V. Zotov[1]

[1] Institute of Geology of Ore Deposits, Petrography, Mineralogy and Geochemistry (IGEM RAS), 35 Staromonetnyi per., 119017 Moscow, Russia

[2] National Research Centre 'Kurchatov Institute', 1 Akademika Kurchatova pl., 123182 Moscow, Russia

[3] ESRF - The European Synchrotron Radiation Facility, CS40220, 38043 Grenoble Cedex 9, France

[4] Helmholtz-Zentrum Dresden-Rossendorf (HZDR), Institute of Resource Ecology, P.O. Box 510119, 01314, Dresden, Germany

[5] Institute of Experimental Mineralogy (IEM RAS), 142432 Chernogolovka, Moscow Region, Russia

[6] Moscow State Geological Prospecting University, 117475, Moscow, Russia

***Corresponding author:** e-mail boris1t@yandex.ru, phone +7-499-2308231

Revised version submitted to Geochimica et Cosmochimica Acta February 2019

ABSTRACT

Hydrothermal chloride-rich fluids are identified at the late stages of the formation of platinum group element (PGE) deposits in giant layered intrusions, and are considered as the PGEs transport media in Cu(-Mo,Au) porphyry systems. In order to quantify the hydrothermal mobility of Pt we performed an investigation of the speciation of Pt in hydrothermal chloride-bearing fluids and dry melt by means of X-ray absorption spectroscopy (XAS). The experiments consisted in recording the Pt L_3-edge X-ray absorption near edge structure/extended X-ray absorption fine structure (XANES/EXAFS) spectra of Pt-bearing fluids obtained by dissolution of Pt metal in KCl/HCl and CsCl/HCl fluids in the temperature range from 450 to 575 °C at pressures from 0.5 to 5 kbar. A spectrum of Pt dissolved in dry CsCl/NaCl/KCl + $K_2S_2O_8$ melt was recorded at 650 °C. The capillary method, when the experimental solution together with $Pt_{(cr)}$ is sealed inside a silica glass capillary, was used. As was determined from the XANES spectra, in all the experimental systems Pt existed in the +2 oxidation state. Analysis of EXAFS spectra showed that Pt is coordinated by four Cl atoms with $R_{Pt\text{-}Cl}$ = 2.31±0.01 Å independently of the *T*-*P*-compositional parameters. No evidence of the formation of complex with alkali metal cations in the second coordination sphere of Pt was found by the analysis of the EXAFS spectra of concentrated CsCl brines and melt. Our results imply that $PtCl_4^{2-}$ is the main Pt-Cl complex which predominates in hydrothermal fluids at t > 400 °C and fluid density d > 0.3 g·cm^{-3}. Experimental data obtained for dry melt of alkali metal chlorides suggest that Pt-Cl complexes can dominate Pt speciation in chloride-bearing aluminosilicate melts where Cl exhibits a salt-like atomic arrangement and ionic bonding. The literature data on the Pt solubility constant, $Pt_{(cr)} + 2\ HCl^\circ_{(aq)} + 2\ Cl^- = PtCl_4^{2-} + H_2{}^\circ_{(aq)}$, are compiled and fitted to the simple density model equation $\log K^\circ_s(PtCl_4^{2-}) = 0.973 - 8202 \cdot T(K)^{-1} - 5.505 \cdot \log d(w) + 2223 \cdot (\log d(w)) \cdot T(K)^{-1}$), where d(w) is the pure water density in g·cm^{-3}. The equation, combined with the extended Debye-Hückel equation for activity coefficients, can be used to calculate the solubility of Pt up to 1000 °C/5 kbar. It accurately predicts the solubility of Pt in concentrated chloride brine (up to 50 wt% NaCl) at parameters of magmatic-hydrothermal transition (800 °C/1.4 kbar). At fluid/vapor density below 0.3 g·cm^{-3} a neutral complex $PtCl_2{}^\circ_{(aq)}$ is suggested as the dominant Pt species. Our data

demonstrate that Pt is highly mobile in high-temperature oxidized chloride-rich hydrothermal fluids. For example, at 800 °C/2 kbar the concentration of Pt can reach a few wt.% in the 1 wt% HCl/50 wt% NaCl fluid which is in equilibrium with magnetite-hematite buffer. Once a Cl-reach fluid exsolves from alumuinosilicate melt, Pt follows Cl and enriches the fluid phase where it exists mostly in the form of $PtCl_4^{2-}$. Decrease of temperature, acidity, and fluid chlorinity results in precipitation of Pt from the fluid phase.

Keywords: platinum, hydrothermal fluids, solubility, chloride complexes, chloride melts, X-ray absorption spectroscopy

1. Introduction

The majority of sulfide deposits of Pt and other platinum-group elements (PGEs) are related to magmatic systems - plutonic and volcanoplutonic complexes among which the layered intrusions host the largest reserves of these metals (e.g. Bushveld Complex, South Africa; Stillwater Complex, Montana, USA; deposits of Norilsk-Talnakh district, Russia). The role of hydrothermal fluids in the formation of these deposits is still debatable. Apart from magmatic hypothesis that considers formation of these deposits as a consequence of the progressive crystallization of one or more magmas or their mixtures, there is another view on the formation of the PGE deposits in the layered intrusions where important role in the concentration of PGEs is assigned to hydrothermal fluids. The possible role of these late mineralizing fluids consists in the formation of the PGEs-bearing reefs as a result of alteration and remelting of the original magmatic mineral assemblages (e.g. Boudreau, 2016; Boudreau, 2017). In all these deposits, hydrothermal fluids were chloride-bearing with the dominant role of NaCl. For example, at the Stillwater Complex the concentration of chloride salts ranged from NaCl-dominated halide melts (>82 wt% NaCl eq., t = 660-800 °C) to more complex Na-Ca-K-Fe-Mn-Ba brines of lower salinity (28-79 wt% NaCl eq., t = 480-640 °C, Hanley et al., 2008). At Merensky reef of the Bushveld Complex salinity of chloride-rich hydrothermal fluids varied from high (60-70 wt% NaCl eq.) to moderate-to-low (20 to ~7 wt% NaCl eq.) depending on the entrapment temperature which was in the range of 750-400 °C (Ballhaus and Strumpfl, 1986; Zhitova et al., 2016). Abundance of H_2O-, Cl-, and F- bearing minerals crystallized in Norilsk ores in the vicinity of the Au-Ag-PGE chalcogenides, chlorides, and intermetallic compounds shows that the ore mineralization was related to post-magmatic hydrothermal stage at temperature <350 °C (Sluzhenikin and Distler, 2015). The PGEs are often extracted as by-products in porphyry Cu(-Mo,Au) deposits where their concentration in sulfide minerals can reach a few hundred ppb level (c.f. Plotinskaya et al., 2018 and references therein). In these deposits oxidized high-temperature (>350 °C) high-salinity (50 wt% and higher) fluids are considered as the transport medium of the PGEs.

Existing experimental data on the state of PGEs in hydrothermal fluids (with emphasis on Pd) implies that Cl is the most important complexing ligand for these elements (e.g., Xiong and Wood, 2000; Boily and Seward, 2005; Boily et al., 2007; Tagirov et al., 2013, Bazarkina and Pokrovski, 2014; Mei et al, 2015). There is a number of experimental determinations of the stability of Pt-Cl complexes published in the literature, but these data are controversial, especially at hydrothermal *T-P* parameters. Gammons et al. (1992) and Tagirov et al. (2015) calculated the $PtCl_3^-$ stability constant using experimental data on the solubility of Pt. In these studies $PtCl_3^-$ was considered as the dominant Pt complex in chloride-bearing fluids at $t \geq 300$ °C. However, as we noted in Tagirov et al. (2015), our experimental data can be affected by interaction of the dissolved metal with the autoclave walls yielding overestimated Pt solubility. To circumvent this we performed a study of the coupled solubility of Au and Pt in chloride-bearing fluids (Zotov et al., 2017). The solubility of the metals was best described by $AuCl_2^-$ and $PtCl_4^{2-}$ complexes. These results are consistent with our recent X-ray absorption (XAS) study of the speciation of Pt in chloride-bearing solutions (Tagirov et al., 2017) where it was demonstrated that $PtCl_4^{2-}$ predominates at 20-350 °C/$P_{sat.}$ at chlorinity from 0.2*m* to 4*m*. Experimental studies of the solubility of Pt in chloride-rich brines and coexisting vapors at the parameters of magmatic-hydrothermal transition also indicate the possibility of the formation of stable Pt-Cl complexes (c.f. Simon and Pettke, 2009). In contrast, Scholten et al. (2018), based on the results of XAS experiments performed at 400-500 °C/800 bar concluded that Pt is practically immobile in Cl-bearing fluids at HCl concentration up to 6.9*m*. Therefore, more experimental data are necessary to provide a basis for reliable thermodynamic model of Pt-Cl complexing in hydrothermal fluids.

The aim of this work is to study the impact of *T-P*-compositional parameters on the Pt speciation by means of synchrotron-based XAS, to combine these data with reliable literature values of the Pt solubility constant, and to quantify the hydrothermal Pt mobility in chloride-bearing fluids at *T-P* parameters from ambient to those of magmatic-hydrothermal transition. The Pt L_3-edge X-ray absorption near edge structure/extended X-ray absorption fine structure (XANES/EXAFS) spectra of HCl/KCl and HCl/CsCl fluids (up to 11*m* of total chloride

concentration) were recorded in situ in the temperature range from 450 to 575 °C at pressures of 500-5300 bar. The X-ray absorption spectrum of Pt in dry CsCl/NaCl/KCl melt was acquired at 650 °C. Combination of these data with Pt solubility constant calculated using literature data for 25-450 °C made it possible to build a model which quantitatively describes the solubility of Pt in Cl-bearing fluids in the wide range of temperatures and pressures – from 25 °C/$P_{sat.}$ to 1000 °C/5000 bar and at fluid salinities at least up to 50 wt% NaCl eq. The model was tested via processing experimental data of Simon and Pettke (2009) on Pt solubility in chloride-rich brine and vapor at 800 °C/1400 bar, and Scholten et al. (2018) on the solubility of Pt in HCl-rich fluid. Both sets of data are in fair agreement with our model. These results provided a basis for discussion of the mechanisms of hydrothermal Pt transport and deposition, and for the estimation of Pt speciation in Cl-bearing aluminosilicate melts.

2. Methods

2.1. X-ray absorption spectroscopy

The Pt L_3-edge X-ray absorption spectra were recorded at the Rossendorf Beamline BM20 (ROBL) of the European Synchrotron Radiation Facility (ESRF) in Grenoble, France. The storage-ring operating conditions were 6.0 GeV and 80-100 mA. The photon energy was scanned from 11310 to 12320 eV using the Si(111) monochromator coupled to Rh-coated mirrors for the collimation and reduction of higher harmonics. Energy calibration was performed using the L_3-edge excitation energy of Pt metal foil (11564 eV). The spectra were collected using 13-element high-throughput Ge-detector. The total energy resolution (incident energy and core − hole lifetime broadening) has been evaluated as 8.8 eV. The detected intensity was normalized to the incident photon flux.

The experimental set-up used for the high-temperature in situ XAS experiments is described in detail in Trigub et al. (2017a,b). A small piece of Pt wire (1.2-1.5 mm long) was loaded into a Polymicro Technologies™ silica glass capillary: 600 μm OD, 250 μm ID, 12 mm length. The capillaries were filled with experimental solutions and hermetically sealed (the capillaries were water-cooled during the sealing). The redox state of the system was controlled

either by sulfite/sulfate equilibrium (experimental solution contained Na_2SO_3/H_2SO_4), or by oxygen produced due to the thermal decomposition of $K_2S_2O_8$ ($K_2S_2O_8 \rightarrow K_2SO_4+SO_2+O_2$). In the latter case a weighted amount (~0.2 g) of KCl + $K_2S_2O_8$ mixture was loaded into the capillary prior to the experimental solution. The HCl concentration was determined by volumetric titration against Trizma® base using methyl red as indicator, and concentration of H_2SO_4 - by densimetry. In case of dry chloride melt the capillaries were loaded with the eutectic mixture of CsCl/NaCl/KCl (30 at% NaCl/24.5 at% KCl with melting temperature of 478 °C) together with $K_2S_2O_8$. The volumetric ratio of the chloride mixture to $K_2S_2O_8$ was ~ 10/1. The capillaries with eutectic chloride mixture were evacuated down to a 10^{-4} bar pressure, sealed, and preconditioned at the experimental temperature during 24 hours. At the beamline a capillary was placed into the microtomography furnace (Bellet et al., 2003) between two plates of silver which eliminated temperature gradient. Temperature readings were calibrated before the experiments at an accuracy of ±5 °C with a *K*-type thermocouple inserted directly in the place of the capillary. Pressure inside the capillary was estimated as following. First, the volumetric degree of filling of the capillary was determined with accuracy of ±3% using optical microscope. Then the mass of solution in the capillary was calculated using tabulated densities of H_2O-CsCl or H_2O-KCl solutions at 25 °C, 1 bar. Finally, the pressure inside the capillary at the experimental temperature was evaluated using *PVT* properties of H_2O-KCl system (Anderko and Pitzer, 1993). We estimate the uncertainty of the calculated pressures as ±25%. This value is based on the uncertainty of the degree of filling of the capillaries. As the *PVT* properties of H_2O-CsCl system at high temperatures are not known, the utilization of the data of the system H_2O-KCl for calculation of experimental pressures of CsCl-bearing fluids also contributes to the overall pressure uncertainty. The spectra were recorded after thermal equilibration of the experimental system and the signal stabilization, which took 30-45 min at the experimental temperature. The parameters of XAS experiments and the experimental fluid compositions are listed in Table 1.

2.2. EXAFS spectra fitting

The EXAFS ($\chi_{exp}(k)$) data were analyzed using ARTEMIS program (a part of IFEFFIT software package, Ravel and Newville, 2005). Following standard procedures for pre-edge subtraction and spline background removal, the structural parameters - interatomic distances (R_i), coordination numbers (N_i), and Debye–Waller factors ($\sigma^2{}_i$) - were determined via the non-linear fit of the theoretical spectra to the experimental ones with the equation

$$\chi(k) = S_0^2 \sum_{i=1}^{n} \frac{N_i F_i(k)}{R_i^2 k} e^{\frac{-2R_i}{\lambda(k)}} e^{-2\sigma_i^2 k^2} \sin\left(2kR_i + \varphi_i(k)\right) \quad . \qquad (1)$$

The theoretical spectra were simulated using photoelectron mean free path length $\lambda(k)$, amplitude $F_i(k)$, and phase shift $\varphi_i(k)$ parameters calculated *ab initio* using the program FEFF6 (Zabinsky et al., 1995).

2.3. Thermodynamic calculations

The standard state of a pure solid phase and H_2O corresponds to a unit activity of the pure phase at a given temperature and pressure. The standard state adopted for the aqueous species is unit activity for a hypothetical one molal ideal solution. The activity coefficients of charged aqueous species were calculated using an extended Debye-Hückel equation

$$\log \gamma_i = -\frac{A z_i^2 \sqrt{I}}{1 + B\,\mathring{a}\sqrt{I}} + \Gamma_\gamma \quad , \qquad (2)$$

where the ion size parameter $\mathring{a}$ was taken to be 4.5 Å for all species, *A* and *B* refer to the Debye-Hückel activity coefficient parameters, *I* is the ionic strength in molal scale, z_i is the charge of the species, and Γ_γ denotes the conversion factor of mol fraction to molality. For neutral species, it was assumed that $\log \gamma_n = \Gamma_\gamma$ = -log (1 + 0.018·m^*) where m* is the sum of the concentrations of all solute species. Speciation calculations were performed by means of the Gibbs computer code of the HCh software package (Shvarov, 2008). Thermodynamic properties of $Pt_{(cr)}$ and aqueous species Na^+, Cl^-, OH^-, HS^-, $H_2S°_{(aq)}$, HSO_4^-, SO_4^{2-}, HSO_3^-, SO_3^{2-}, $S_2O_3^{2-}$, K^+, $NaOH°_{(aq)}$, $KOH°_{(aq)}$, Cs^+, $CsCl°_{(aq)}$, $CsOH°_{(aq)}$, and other oxidized sulfur species were taken from SUPCRT92 database (Johnson et al., 1992), for CsCl° - from Sverjensky et al. (1997).

Thermodynamic properties of H_2O and HCl° from Wagner and Pruss (2002) and Tagirov et al. (1997), respectively; those of $H_2°_{(aq)}$, $O_2°_{(aq)}$, and $SO_2°_{(aq)}$ - from Akinfiev and Diamond (2003), data for $NaCl°_{(aq)}$ and $KCl°_{(aq)}$ – from Ho et al. (1994) and Ho and Palmer (1997), respectively. The values of Henry constants, dissociation constants of aqueous electrolytes calculated using the aforementioned thermodynamic data (except data available at SUPCRT database) are presented in Electronic Annex together with corresponding values of Gibbs fee energies of aqueous species (Tables EA1-EA10). Thermodynamic properties of hematite Fe_2O_3, magnetite Fe_3O_4, $Ni_{(cr)}$, and bunsenite NiO were taken from Robie and Hemingway (1995).

In order to compare the Pt solubility model obtained in the present study with experimental data on the solubility of Pt in coexisting vapor-brine-rhyolite melt system (Simon and Pettke, 2009), the chemical speciation of solutes and the solubility of Pt in coexisting brine and vapor phases of the H_2O - NaCl system were calculated using the method developed in Akinfiev and Diamond (2009) for computation of SiO_2 solubility in H_2O - salt systems. In this method an *effective* H_2O molar volume $V^*_{H_2O}$ (which corresponds to *effective* pressure $P_{\text{eff.}}$) is used instead of the pure water volume $V^{o}_{H_2O}$. The value of $V^*_{H_2O}$ is computed for given *T-P* parameters and total NaCl content from the equation

$$V_{mix} = X_{H_2O} V^*_{H_2O} + X_{NaCl} V_{NaCl} \qquad (3)$$

where V_{mix} is the molar volume of the H_2O - NaCl fluid ($cm^3 \cdot mol^{-1}$), and X_{NaCl} and V_{NaCl} denote the mole fraction and the intrinsic volume of the solute, NaCl, respectively. The V_{mix} was adopted from the Driesner and Heinrich (2007) H_2O - NaCl equation of state (EoS), while for pure NaCl V_{NaCl} = 30.8 $cm^3 \cdot mol^{-1}$ was used (Akinfiev and Diamond, 2009). In some of the experiments of Simon and Pettke (2009) the experimental system contained Ag/AgCl buffer which controlled the activity of HCl. To model the Ag-bearing system, thermodynamic properties of $AgCl_2^-$ (Tagirov et al., 1997), $AgCl°_{(aq)}$ (Akinfiev and Zotov, 2016), and other Ag species (Akinfiev and Zotov, 2010) were used. Activity of Ag in Pt-Ag alloy was taken equal to Ag mole fraction $a(Ag) = X(Ag) = 0.7$ (Okamoto, 1997).

3. Results

3.1. Quantitative analysis of XANES spectra

The Pt L_3-edge XANES spectra are presented in Fig. 1a. Positions of the main spectral features are given in Table 2. The spectra of Pt in experimental solutions and melt differ from the spectra of Pt(IV) references – H_2PtCl_6 and K_2PtCl_6. At the same time, position of the absorption edge (or edge jump, e.j.) and white line (the first intensive peak of the spectrum, WL) of the experimental systems are identical to the Pt(II) reference K_2PtCl_4. Therefore, the formal oxidation state of Pt is +2 in all the experimental fluids and chloride melt despite high oxygen fugacity.

3.2. EXAFS spectra fitting

The Pt L_3-edge EXAFS spectra and their Fourier Transforms are shown in Fig. 1b and c, respectively. Results of the EXAFS spectra fitting are presented in Table 3 and shown in Fig. 2 (Experiments Cap 2160 and Cap 120) and Fig. EA1 (Experiments Cap 119, Cap 125). In all studied systems the best fits of experimental spectra were achieved for the model with four Cl atoms in the 1st coordination sphere of Pt. The interatomic distances in the 1st coordination sphere are independent of the *T*-*P*-compositional parameters. Attempts to replace a Cl atom with O always resulted in the oxygen-free 1st coordination sphere. Therefore, only Cl presents in the first coordination sphere of Pt, and $PtCl_4^{2-}$ is the dominant Pt complex.

In order to explore the possibility of the alkali metal atom (Me) to present in the second coordination sphere of Pt and to contribute to the EXAFS signal we performed two fits of each spectra. The first model included the alkali metal atom (left panels in Table 3 and Fig. 2, Fig. EA1), whereas the second fit was performed without the Pt-Me path (right panels in Table 3 and Fig. 2, Fig EA1). In general, inclusion of the second-coordination-sphere atom had negligible effect on the fit quality. In some cases, however, the fine structure of the EXAFS spectra in the region between 3 and 4 Å (not corrected for phase shift) was better described when the Pt-Me path was included into the fit (for example, for Cap 120 experiment). This data indicate that, even when the alkali metal cation presents in the second coordination sphere of Pt, it does not

form a stable complex of rigid geometry (as in this case its contribution would be clearly distinguishable), but has a diffuse distribution similar to the Au-Cl complexation (Mei et al., 2014; Tagirov et al., 2019). As the cation has no effect on the fit results for the 1st coordination sphere, any model presented in Table 3 can be used to characterize the nearest neighbors of Pt.

The Pt-Cl coordination numbers and distances in the 1st coordination sphere (N_{Cl} = 4.0±0.7, $R_{Pt\text{-}Cl}$ = 2.31±0.01 Å) are similar to those described in our previous study of Pt-Cl complexing (Tagirov et al., 2017), where the local atomic environment of Pt was determined at 20-350 °C in solutions of 1.5*m* HCl, 0.2*m* HCl/0.8*m* NaCl, and 0.2*m* HCl/4*m* NaCl. Therefore, $PtCl_4^{2-}$ predominates in the wide range of system parameters, from ambient *T-P* parameters to those of magmatic-hydrothermal transition, and at system chlorinities from ca. 1*m* of total chloride concentration to anhydrous chloride melt.

3.3. Pt solubility constant, $K_s°(PtCl_4^{2-})$, at 25 – 1000 °C, P_{sat} – 5000 bar

The speciation of Pt in chloride-bearing fluids, according to the EXAFS data, corresponds to $PtCl_4^{2-}$. In the present section stability of this complex is evaluated using literature data on the solubility of Pt. Three sources of stability constants for $PtCl_4^{2-}$ were used (Table 4). For low temperatures and pressures, $t \leq 150$ °C, $P_{sat.}$, we adopted the Pt solubility constant

$$Pt_{(cr)} + 2\,HCl°_{(aq)} + 2\,Cl^- = PtCl_4^{2-} + H_{2(aq)} \qquad K_s(PtCl_4^{2-}) \qquad (4)$$

reported in compilation of Tagirov et al. (2015). This compilation is based on the potentiometric studies of $PtCl_4^{2-}$ stability at 25 and 60 °C/$P_{sat.}$ performed by Ginstrup (1972), and at 25-150 °C/$P_{sat.}$ by Nikolaeva and Erenburg (1977). The partial molal volume $V°(PtCl_4^{2-})$ = 73.28 $cm^3 \cdot mol^{-1}$ calculated using data of Kawaizumi (1992) was included into the set of the experimental data. For elevated temperatures and pressures of 350-450 °C/500-1000 bar we used results of our recent study of the coupled solubility of Au and Pt in chloride-bearing fluids (Zotov et al., 2017). In this study it was demonstrated that at the listed above *T-P* parameters and fluid chlorinities from 0.2*m* to 1*m* the solubilities of Au and Pt are consistent with the reaction,

$$2\ Au_{(cr)} + PtCl_4^{2-} = Pt_{(cr)} + 2\ AuCl_2^- \qquad K_{(Pt\text{-}Au)}\ , \qquad (5)$$

with reaction constant independent of the system physical-chemical parameters (pH, fluid chlorinity and redox potential),

$$\log K°_{(Pt\text{-}Au)} = 2 \log a(AuCl_2^-) - \log a(PtCl_4^{2-}) + \log a(Pt_{(cr)}) - 2 \log a(Au_{(cr)})\ . \qquad (6)$$

The values of $\log K°_{(Pt\text{-}Au)}$, together with the values of $AuCl_2^-$ solubility constant

$$Au_{(cr)} + HCl°_{(aq)} + Cl^- = AuCl_2^- + H_{2(aq)} \qquad K_s(AuCl_2^-) \qquad (7)$$

from Zotov et al. (2018) were used to evaluate the Pt solubility constant $K°_s(PtCl_4^{2-})$ (Eq. 4). The values of $K°_s(AuCl_2^-)$ used in the calculation are given in Table EA11, and the values of Gibbs free energy (*g*) of the complex are listed in Table EA12. The resulting Pt solubility constants (Table 4) were fitted to a simple density model equation (Anderson et al., 1991),

$$\log K_s°(PtCl_4^{2-}) = 0.973 - 8202 \cdot T(K)^{-1} - 5.505 \cdot \log d(w) + 2223 \cdot (\log d(w)) \cdot T(K)^{-1})\ , \qquad (8)$$

where d(w) is the pure water density in $g \cdot cm^{-3}$. The calculated values of $K°_s(PtCl_4^{2-})$ are listed in Table 5, and the corresponding values of Gibbs free energy of $PtCl_4^{2-}$ are given in Table EA13. The calculated solubility constants, $K_s°(PtCl_4^{2-})$, are plotted in Fig. 3 together with the literature experimental data. An important feature of the Pt solubility constant ($\log K_s(PtCl_4^{2-})$) is its proximity to linear character with respect to the reciprocal temperature. Therefore, the range of the temperatures where Eq. (8) can be used to calculate the Pt solubility was extended up to 1000 °C.

4. Discussion

4.1. Speciation of Pt in hydrothermal systems and anhydrous chloride melts

Our data demonstrate that the speciation of Pt in chloride-bearing fluids corresponds to $PtCl_4^{2-}$ in wide range of *T-P*-compositional parameters of the Earth crust and the upper mantle, from subcritical temperatures to parameters of magmatic-hydrothermal transition, and from relatively diluted acidic chloride fluids of ca. 0.2*m* total chloride to dry chloride melt. In these

fluids the solubility of Pt is described by Eq. (4), or, involving the proton activity (or pH = -log $a(H^+)$),

$$Pt_{(cr)} + 2\ H^+ + 4\ Cl^- = PtCl_4^{2-} + H_{2(g)} \quad , \quad (9)$$

or, using oxygen as a reactant which acts as an oxidizing agent,

$$Pt_{(cr)} + 2\ HCl°_{(aq)} + 2\ Cl^- + 0.5\ O_{2(g)} = PtCl_4^{2-} + H_2O \quad . \quad (10)$$

Similar reaction can be written for Pt dissolution in dry chloride melt,

$$Pt_{(cr)} + 4\ Cl^- + 0.5\ O_{2(g)} = PtCl_4^{2-} + O^{2-} \quad , \quad (11)$$

or, in terms of Na-bearing species,

$$Pt_{(cr)} + 2\ NaCl + 2\ Cl^- + 0.5\ O_{2(g)} = PtCl_4^{2-} + Na_2O \quad . \quad (12)$$

Reactions (4) and (9)-(12) show that the solubility (concentration) of Pt in chloride-bearing fluids, brines, and melts increases proportionally to the 2nd power of fluid acidity, the 4th power of chloride activity (or, in rough, the total chloride salt concentration), and decreases proportionally to the hydrogen fugacity (or increases proportionally to $f(O_2)^{0.5}$). The literature data on the solubility of Pt in sulfide-bearing systems imply that the other important species that can afford the transport of Pt at subcritical temperatures and low fluid chlorinity are hydrosulfide complexes ($Pt(HS)_2°$ and $Pt(HS)_3^-$, e.g. Gammons and Bloom, 1993; Kokh et al., 2017).

Identity of the speciation of Pt in wide range of Cl concentration implies that the solubility of Pt can be calculated using reaction (4) constant, $K_s(PtCl_4^{2-})$, at any set of *T*-*P*-compositional parameters of the natural ore-forming fluids, from diluted low-temperature solutions to concentrated magmatic-hydrothermal fluids. In such calculations the effect of dissolved chloride salts on the solubility of Pt can be explicitly accounted for by the activity coefficients calculated by means of the extended Debye-Hückel equation even in the case of concentrated brines. In low-density fluids (d < 0.3 g·cm^{-3}) the $PtCl_2°$ is expected to be the dominant Pt species (see the next section). Some examples of these thermodynamic calculations are given in the following sections.

Anhydrous chloride salt melts as a reservoir which accumulates metals at the upper part of degassing magma chamber beneath volcanoes was suggested by Shmulovich and Churakov (1998) and Shmulovich et al. (2016) to explain formation of the metal-rich fumarolic products.

For example, Pd-Pt selenide and native Pt were discovered in artificial fumarolic preciptates sampled at Kudryavy volcano (Kurile Islands) (Korzhinsky et al., 1996; Yudovskaya et al., 2006). At this volcano high PGEs concentrations were established in mineralized rocks and fumarolic gas condensates (a few tens ppb to 0.5 ppm Pt, up to 8 ppm Pd, and 1 ppm Os, Distler et al., 2002). Formation of lenses of high-salinity brine is suggested in Afanasyev et al. (2018) to explain regions of high electrical conductivity beneath active and dormant volcanoes. Results of our study imply that these melts and brines can accumulate high concentrations of Pt in the form of $PtCl_4^{2-}$ (Reactions 11, 12) which is transported to the earth surface by high-temperature low-density fumarolic gases in the form of $PtCl_2°_{(aq)}$.

4.2. Comparison of calculated Pt solubility in magmatic-hydrothermal fluids with the literature data

Simon and Pettke (2009) determined the solubility of Pt in coexisting Cl-bearing vapor, brine, and rhyolite melt at 800 °C. The hydrogen fugacity was controlled by Ni-NiO buffer. Two series of experiments were performed: at pressure of 1400 bar the HCl activity was controlled by Ag/AgCl buffer, whereas at 1000 bar pressure the HCl activity was not buffered. The experimental data reported in Simon and Pettke (2009) were used to test our thermodynamic model of Pt solubility. Comparison of the experimental and calculated Pt solubility is given in Table 6; results of the speciation calculations are presented in Tables EA14-EA17. In the system with HCl activity buffered by Ag/AgCl couple (P = 1400 bar, Calculations A and B in Table 6) the experimental Pt solubility values agree within 0.3 log units with the concentration of $PtCl_4^{2-}$ in both brine and vapor phases. Close agreement between the experiment and the model predictions for $PtCl_4^{2-}$ argues for high accuracy of our model of Pt speciation and solubility, as well as of thermodynamic properties of Ag-Cl aqueous complexes which affect the speciation of Cl due to high solubility of liquid AgCl at the experimental *T-P* parameters. High NaCl concentration in dense brine results in higher Pt content compared to the low density vapor with much lower NaCl concentration (the difference is ca. 30 times at 1400 bar, Calculations A and B). In the case of unbuffered with respect to HCl brine (P = 1000 bar, Calculation C) the HCl

concentration of 2.8*m* (mol·(kg H_2O)$^{-1}$) estimated by Simon and Pettke (2009) yields the dissolved Pt concentration 160 times higher than the measured value. To get the correct value of Pt solubility in unbuffered with respect to HCl activity brine the HCl concentration of 0.22*m* should be used (Calculation E). Calculation F shows that the measured concentration of Pt in the low-density vapor phase is much higher than the $PtCl_4^{2-}$ concentration calculated using Eq. 8 for log $K_s°(PtCl_4^{2-})$. This means that another Pt-Cl complex becomes dominant in the low-density phase which results in increase of dissolved Pt concentration. As the concentration of NaCl in the vapor phase is much lower than that in brine, and neutral species become much more important due to enhancement of ionic association at low densities, it is expected that the neutral $PtCl_2°_{(aq)}$ complex predominates in the vapor phase. The value of Gibbs energy $g(PtCl_2°_{(aq)})$ = -298.7 kJ·mol^{-1} fits accurately the experimental Pt solubility in the low-density vapor (Calculation F). Assuming that the partial molal volume $V°(PtCl_2°_{(aq)}) \sim V°(PdCl_2°_{(aq)})$ (Table 6 in Tagirov et al., 2015) we got the equilibrium concentration in the coexisting brine $m(PtCl_2°_{(aq)}) \sim 3.8 \cdot 10^{-7}$ mol·(kg H_2O)$^{-1}$ which is negligible in comparison with the measured Pt concentration of $5.0 \cdot 10^{-5}$*m* accounted for by the presence of $PtCl_4^{2-}$. This calculation yields the Pt solubility constant for 800 °C/1000 bar,

$$Pt_{(cr)} + 2\,HCl°_{(aq)} = PtCl_2°_{(aq)} + H_{2(aq)} \qquad K°_s(PtCl_2°_{(aq)}) = 10^{-6.4} \qquad (13)$$

or, when reaction involves the gas phase H_2,

$$Pt_{(cr)} + 2\,HCl°_{(aq)} = PtCl_2°_{(aq)} + H_{2(g)} \qquad K°_s*(PtCl_2°_{(aq)}) = 10^{-5.0} \qquad (14)$$

Further extrapolation of $g(PtCl_2°_{(aq)})$ to the system with Ag/AgCl buffer results in $PtCl_2°_{(aq)}$ concentration in vapor phase commensurable with the concentration of $PtCl_4^{2-}$ (last column in Table 6, Calculation B). We note, however, that the values of $g(PtCl_2°_{(aq)})$ and the calculated concentrations of $PtCl_2°_{(aq)}$ are the rough estimates only. The accurate determination of the $PtCl_2°_{(aq)}$ stability needs further experimental investigation.

Scholten et al. (2018) determined the solubility of Pt using results of X-ray fluorescence measurements. A glassy carbon cell was used in the experiments. It was determined that at 500 °C/800 bar 12.8 ppm Pt ($8 \cdot 10^{-5}$*m*) was dissolved in 6.86*m* HCl. At lower HCl concentration of 1*m*, as well as in equilibrium with sperrylite ($PtAs_2$), the Pt concentration was below the

detection limit. To model the Pt solubility experiment of Scholten et al. (2018) we performed two calculations. The *T-P* parameters were set as 500 °C/1000 bar. In the first calculation the system was unbuffered with respect to oxygen fugacity, whereas in the second one the $f(O_2)$ was controlled by reactions of dissolution of graphite with the formation of $CO_{(aq)}$, $CO_{2(aq)}$, and $CH_{4(aq)}$ (thermodynamic properties of all these substances were taken from SUPCRT92 database). The calculated $PtCl_4^{2-}$ concentration in $f(O_2)$ unbuffered system was $6 \cdot 10^{-5} m$ which is in excellent agreement with results of Scholten et al. (2018) ($8 \cdot 10^{-5} m$). In equilibrium with graphite the $PtCl_4^{2-}$ concentration decreased by 3 orders of magnitude due to decrease of the redox potential. Therefore, we can conclude that the equilibrium with graphite was not attained in the experiments of Scholten et al. (2018), and the measured solubility of Pt was accounted for by the formation of $PtCl_4^{2-}$. Experiments of Scholten et al. (2018) were performed in the salt-free system where the solubility of Pt is low because $HCl°_{(aq)}$ is the dominant form of chloride (in 6.9 *m* HCl at 500 °C/1000 bar the concentration of free Cl^- ion is 0.1*m*). In the presence of chloride salts the concentration of Pt increases sharply (Eqs. 9, 10).

4.3. The solubility of Pt in chloride-bearing fluids and Au/Pt ratio

The solubility of Pt is shown in Fig. 4a in terms of the concentrations of individual complexes. As follows from the reaction (9) stoichiometry, the concentration of $PtCl_4^{2-}$ increases proportionally to the second power of fluid acidity (at constant chloride concentration). Therefore, the slope of the lines corresponding to the concentration of $PtCl_4^{2-}$ vs. pH in Fig. 4a is close to -2. The concentration of the Pt-Cl complex increases sharply with increasing temperature. For example, at pH = 2 the concentration of $PtCl_4^{2-}$ increases by 11 orders of magnitude with increase of the temperature from 200 to 400 °C and reaches 0.01 ppb in 1*m* NaCl (6 wt%) in equilibrium with Ni-NiO redox buffer. The concentration of Pt-HS complexes, in contrast, depends weakly on the temperature. Experimental data available on the solubility of $PtS_{(cr)}$ (cooperite) in hydrothermal fluids are consistent with the presence of two Pt-HS complexes: $Pt(HS)_2°$ and $Pt(HS)_3^-$. The concentration of the former, which dominates in acidic fluids where $H_2S°_{(aq)}$ is prevalent, is independent of pH, whereas the concentration of the latter

has a maximum at near-neutral pH with pH = pK_{H_2S}. Stability of $Pt(HS)_3^-$ decreases with increasing temperature. Therefore, the maximum on the solubility curve is clearly distinguishable only at 200 °C and disappears at 300 °C. At the concentration of reduced sulfur of 0.01*m* (320 ppm) and temperature between 200 and 450 °C the concentration of Pt-HS complexes varies between 10 ppt and 0.5 ppb. As the effect of temperature on the stability constant is much more pronounced for $PtCl_4^{2-}$, at t > 400 °C Pt-HS complexes in acidic fluids become negligible compared to $PtCl_4^{2-}$. As follows from Fig. 4a, the concentration of Pt at parameters of magmatic-hydrothermal transition (t > 600 °C) can be very high even in relatively diluted fluids with reduced redox state imposed by the Ni-NiO buffer. For example, at 800 °C in near-neutral fluids the concentration of $PtCl_4^{2-}$ is 1 ppm, and decrease of pH by one log unit yields 10^2 fold increase of the Pt solubility. Accordingly, decrease of temperature, redox potential, and acid neutralization result in precipitation of dissolved Pt. Besides, precipitation of Pt can result from the increase of activity of reduced S and other chalcogens (Se, Te) and pnictogens (As, Sb, Bi) which form stable solid phases with Pt.

Dependence of the solubility of Pt on the fluid acidity, concentration of NaCl and redox state is illustrated in Fig. 4b for parameters of magmatic-hydrothermal transition (800 °C, 2 kbar). The concentration of Pt in fluid which contains 50 wt% NaCl and 1 wt% HCl increases from 150 ppm to 2.5 wt% with $f(O_2)$ change from reducing (Ni-NiO) to oxidizing (Fe_3O_4-Fe_2O_3) conditions.

The effect of the fluid chlorinity, redox state and temperature on the solubilities of Au and Pt are compared in Fig. 5a,b. The slope of the solubility curves as a function of fluid chlorinity is controlled by the composition of the dominant complexes: $AuOH°/AuCl_2^-$ and $PtCl_4^{2-}$. The extended flat part of Au solubility curve is explained by predominance region of AuOH°. Since there is no data on the stability of Pt-OH complex, we did not include it in the calculation and, therefore, the Pt solubility curve starts to increase at lower fluid chlorinity. The solubility of Pt increases much more sharply with increase of NaCl concentration as the number of Cl ligands in $PtCl_4^{2-}$ complex is twice as much as that in the $AuCl_2^-$. Increase of the redox potential from Ni-NiO to Fe_3O_4-Fe_2O_3 buffer results in increase of the solubility of ca. 10^2 times

for Pt and 10 times for Au. The difference between the concentrations of Au and Pt decreases with increasing temperature, especially in concentrated chloride brines (contrast to the low-density fluids, see below). At 800 °C/2000 bar and *C*(NaCl) = 50 wt% the concentration of dissolved Pt is only 2.5 log units lower than the concentration of Au, whereas at *C*(NaCl) = 0.1 wt% the difference is 7 log units.

Figure 6 illustrates the effect of *T*-*P* parameters on the Au/Pt ratio in chloride-bearing fluids. The factors that decrease the Au/Pt ratio, or, in other words, lead to Pt enrichment of the fluid and deposited ores are:

(i) an increase of the temperature in the region of high to moderate fluid densities. However, in the fluids of low density (the pure water density below 0.4 $g \cdot cm^{-3}$, this region corresponds to $t > 600$ °C in Fig. 6) the dependence of the Au/Pt ratio vs. *T* inverses and the ratio increases with increasing temperature;

(ii) an increase of the NaCl concentration.

4.4. Speciation of Pt in chloride-bearing magmas

Another important consequence of the present study concerns the state of Pt in silicate melts. Experiments on the solubility of Pt in Cl-free silicate melts of different composition (Borisov and Palme, 1997) demonstrated that the dissolved Pt concentration increases proportionally to the $f(O_2)^{0.5}$,

$$Pt_{(cr)} + 0.5\ O_{2(g)} = PtO_{(melt)} \quad (15)$$

which means that the "formal" oxidation state of Pt in silicate melts is +2. At the same time, the silicate melts contain halogens and sulfur which are important complexing ligands for Pt and other PGEs. The positive oxidation state of Pt in Cl-free melts implies the possibility of the formation of Pt^{2+}-Cl^- complexes in Cl-bearing systems. The concentration of Cl in magmas varies from a few ppm to 1-2 wt% depending on the melt composition and history (i.e., partial melting and the concentration of Cl at the source of melting, fractional crystallization, magma mixing and so on, see review of the magmatic halogen chemistry in Webster et al., 2018). Spectroscopic studies of the speciation of Cl in aluminosilicate glasses indicate that Cl is mostly

coordinated by network-modifying cations (Na, Ca, Mg, Ba and so on), without clear contribution of network-forming Al and Si (Webster et al., 2018). Results of XANES study of the speciation of Cl in silicate glasses reported in Evans et al. (2008) showed that "there are similarities between spectra from Ca-bearing melts and the spectra of hydrated $CaCl_2 \cdot 2H_2O$, suggesting that the Ca-Cl_x species could have a salt-like atomic arrangement and ionic bonding." Investigation of quench products of KCl-bearing carbonate-silicate melts by means of Raman and XANES spectroscopies demonstrated that Cl predominantly presents as $(K_xNa_{1-x})Cl$ complexes with a distinct contribution of free Cl^- ion (Safonov et al., 2017). These data suggest that the speciation of Cl in aluminosilicate melts, at least to some extent, is similar to the state of Cl in anhydrous chloride melts and aqueous brines. Therefore, our experimental data on the speciation of Pt also can be used to constrain the Pt speciation model in Cl-bearing aluminosilicate melts.

Experimental determination of the solubility of Au in Cl- and S-bearing hydrous melts of rhyodacitic to andesitic compositions demonstrated direct correlation between the dissolved Au concentration and the concentrations of Cl and S (Botcharnikov et al., 2010). Increase of concentration of dissolved Cl to 1 wt% lead to increase of the solubility of Au by a factor of five compared to the Cl-free system. At the same time, no effect of H_2O content on the Au solubility was observed. These results lead the authors to the conclusion that Au may form complexes with Cl and S in silicate melts. Results of our study confirm this finding and extend it to the case of Pt and, probably, the other PGEs. Both Au and Pt in dry alkali metal chloride melts exist in the form of chloride complexes $AuCl_2^-$ (Tagirov et al., 2019) and $PtCl_4^{2-}$ (this study). Comparison of our data with experimental results of Botcharnikov et al. (2010) for the solubility of Au in Cl-bearing silicate melts, and Evans et al. (2008) and Safonov et al. (2017) for the speciation of Cl in quench products of silicate melts lead to conclusion that Au and Pt chloride complexes can dominate the speciation of these metals not only in chloride-rich aqueous fluids and anhydrous chloride melts, but in chloride-bearing silicate melts as well. In this case the solubility of Pt will be controlled by activity (concentration) of Cl and the redox state (oxygen fugacity) according to

Reactions (11) and (12). As the concentration of Cl in silicate melts is low, formation of Pt-Cl complexes with lower number of ligands is possible (for example, $PtCl_3^-$ and $PtCl_2°$).

Another possible important species which can dominate the speciation of Pt, other PGEs and Au in silicate melts are complexes with sulfur-bearing ligands. For example, Botcharnikov et al. (2011) found that Au can be mobilized in the sulfur-bearing silicate melts at redox conditions of sulfide-sulfate transition (when the concentrations of S^{2-} and S^{6+} are close to each other). In such a case the concentration of Au exhibits a maximum when it is complexed with S^{2-} ion or with other S-bearing ligands, including species in transitional oxidation states like S_3^- which is abundant component of hydrothermal fluids (Pokrovski and Dubessy, 2015; Barré et al., 2017) and can also present in silicate melts. Similar complexes can be formed by Pt.

At parameters of magmatic-hydrothermal transition the partition coefficient $D_{Cl}^{fluid/melt} > 1$ (Botcharnikov et al., 2015), i.e. Cl partitions to the fluid phase. Our data imply that Pt follows Cl and enriches the fluid phase where it exists mostly in the form of $PtCl_4^{2-}$ or $PtCl_2°$ (the latter can dominate at fluid/vapor density $d < 0.3$ g·cm^{-3}). As the temperature decreases, the Pt-HS complexes also contribute to hydrothermal transport of Pt (Fig. 4a). However, the available thermodynamical data on the stability of Pt-HS species are insufficient to quantify their impact on the hydrothermal transport of Pt: determination of the stability of Pt-HS complexes is ongoing study in our laboratory.

5. Conclusions

In the present study we recorded Pt L_3-edge X-ray absorption spectra of aqueous chloride-bearing fluids (7*m* HCl/4*m* CsCl and 4*m* HCl/6*m* KCl) at temperatures 450-575 °C and pressures up to 5000 bar. X-ray absorption spectrum of dry CsCl/NaCl/KCl melt was recorded at 650 °C. The capillary method, where the experimental solution together with a solid phase (Pt) is sealed inside a silica glass capillary, was used for the experiments. Interpretation of the EXAFS spectra showed that in all the experimental systems $PtCl_4^{2-}$ predominates the Pt speciation. The distance between Pt and the nearest-neighbor Cl atoms is 2.31±0.01 Å. The fact that this complex presents in high concentration in dry melt of the alkali metal chlorides indicates the

possible important contribution of Pt-Cl complexing in Pt transport by chloride-bearing aluminosilicate melts, where Cl could have a salt-like atomic arrangement and ionic bonding. Available literature data on the Pt solubility constant with the formation of $PtCl_4^{2-}$ (25-450 °C, $P_{sat.}$-1000 bar) were compiled and fitted to a simple density model equation. The equation, combined with the extended Debye-Hückel equation for activity coefficients of ionic species, can be used to predict Pt solubility in chloride-bearing fluids up to 1000 °C at pressures up to 5000 bar. Comparison of the calculated Pt solubility with the experimental data published so far demonstrates that the solubility of Pt can be accurately calculated in the wide range of fluid chlorinities including concentrated brines (50 wt% NaCl) at *T-P* parameters of magmatic-hydrothermal transition. Thermodynamic calculations performed using the obtained results showed that the formation of $PtCl_4^{2-}$ can account for efficient hydrothermal transport of Pt at $t >$ 400 °C. For example, at temperature of 800 °C the solubility of Pt in oxidized chloride-rich fluids and brines can reach a few tens ppm to one wt% level depending on the acid concentration. At $t <$ 400 °C, in sulfide-bearing fluids with moderate salt concentration of a few wt% NaCl eq. hydrosulfide complexes become the dominant Pt species which concentration varies from a few ppt to a few tenths of ppb.

Acknowledgements

The authors acknowledge the ESRF for the beamtime allocation under proposals 20-01-782 (BM20 beamline). We thank Joerg Exner for technical support during the in-situ experiment with a micro-tomo furnace at BM20. Pavel Selivanov is acknowledged for preparation of capillaries. We thank Max Wilke and Elena Bazarkina for providing us with silica glass capillaries. We are grateful to LaurenTruche and anonymous reviewer for helpful reviews of the manuscript. Chemical analyses were carried out at the “IGEM-Analytica” Center of collective use. This study was supported by the Russian Science Foundation grant No. 17-17-01220 (spectroscopic experiment and interpretation) and Basis theme IGEM RAS (thermodynamic calculations).

References

Afanasyev A., Blundy J., Melnik O., Sparks S. (2018) Formation of magmatic brine lenses via focussed fluid-flow beneath volcanoes. *Earth Plan. Sci. Let.* **486,** 119–128.

Akinfiev N.N. and Diamond L.W. (2003) Thermodynamic description of aqueous nonelectrolytes at infinite dilution over a wide range of state parameters. *Geochim. Cosmochim. Acta* **67,** 613-627.

Akinfiev N.N. and Diamond L.W. (2009) A simple predictive model of quartz solubility in water–salt–CO_2 systems at temperatures up to 1000 °C and pressures up to 1000 MPa. *Geochim. Cosmochim. Acta* **73,** 1597–1608.

Akinfiev N.N. and Zotov, A.V. (2010) Thermodynamic description of aqueous species in the system Cu-Ag-Au-S-O-H at temperatures of 0-600°C and pressures of 1-3000 bar. *Geochem. Int.* **48,** 714-720.

Akinfiev N.N. and Zotov A.V. (2016) Solubility of chlorargyrite (AgCl(cr./l.)) in water: New experimental data and a predictive model valid for a wide range of temperatures (273–873K) and water densities (0.01–1g·cm^{-3}). *Geochim. Cosmochim. Acta* **178,** 178-194.

Anderko A. and Pitzer K.S. (1993) Phase equilibria and volumetric properties of the systems KCl-H_2O and NaCl-KCl-H_2O above 573 K: Equation of state representation. *Geochim. Cosmochim. Acta* **57,** 4885-4897.

Anderson G.M., Castet S., Schott J. and Mesmer R.E. (1991) The density model for estimation of thermodynamic parameters of reactions at high temperatures and pressures. *Geochim. Cosmochim. Acta* **55,** 1769-1779.

Ballhaus C.G. and Stumpfl E.F. (1986) Sulfide and platinum mineralization in the Merensky Reef: evidence from hydrous silicates and fluid inclusions. *Contrib. Mineral. Petrol.* **94,** 193-204.

Barré G., Truche L., Bazarkina E., Michels R. and Dubessy J. (2017) First evidence of the trisulfur radical ion S_3^- and other sulfur polymers in natural fluid inclusions. *Chem. Geol.* **462,** 1-14.

Bazarkina E.F., Pokrovski G.S. and Hazemann J.-L. (2014) Structure, stability and geochemical role of palladium chloride complexes in hydrothermal fluids. *Geochim. Cosmochim. Acta* **146,** 107-131.

Bellet D., Gorges B., Dallery A., Bernard P., Pereiro E. and Baruchel J. (2003) A 1300 K furnace for in situ X-ray microtomography. *J. Appl. Cryst.* **36,** 366-367.

Boily J.-F. and Seward T.M. (2005) Palladium(II) chloride complexation: Spectrophotometric investigation in aqueous solutions from 5 to 125°C and theoretical insight into Pd-Cl and Pd-OH_2 interactions. *Geochim. Cosmochim. Acta* **69,** 3773-3789.

Boily J.-F., Seward T.M., Charnock J.M. (2007) The hydrolysis and precipitation of Pd(II) in 0.6 mol kg^{-1} NaCl: A potentiometric, spectrophotometric, and EXAFS study. *Geochim. Cosmochim. Acta* **71,** 4834-4845.

Borisov A. and Palme H. (1997) Experimental determination of the solubility of platinum in silicate melts. *Geochim. Cosmochim. Acta* **61,** 4349-4357.

Botcharnikov R.E., Linnen R.L. and Holtz F. (2010) Solubility of Au in Cl- and S-bearing hydrous silicate melts. *Geochim. Cosmochim. Acta* **74,** 2396–2411.

Botcharnikov R.E., Linnen R.L., Wilke M., Holtz F., Jugo P.J. and Berndt J. (2011) High gold concentrations in sulphide-bearing magma under oxidizing conditions. *Nature Geoscience* 4, 112-115.

Botcharnikov R.E., Holtz F. and Behrens H. (2015) Solubility and fluid–melt partitioning of H_2O and Cl in andesitic magmas as a function of pressure between 50 and 500 MPa. *Chem. Geol.* **418,** 117–131.

Boudreau A.E. (2016) The Stillwater Complex, Montana – overview and the significance of volatiles. *Min. Mag.* **80,** 585-637.

Boudreau A.E. (2017) A personal perspective on layered intrusions. *Elements* **13,** 380-381.

Distler V.V., Yudovskaya M.A., Znamenskii V.S. and Chaplygin I.V. (2002) Platium group elements in modern fumaroles of the Kudryavyi volcano, Iturup island, Kuril island arc. *Doklady Earth Sciences* **387**(8), 975-978.

Driesner T. and Heinrich C.A. (2007) The system H_2O–NaCl. Part I: Correlation formulae for phase relations in temperature–pressure–composition space from 0 to 1000 °C, 0 to 5000 bar, and 0 to 1 X_{NaCl}. *Geochim. Cosmochim. Acta* **71,** 4880–4901.

Evans K.A., Mavrogenes J.A., O'Neill H.S., Keller N.S. and Jang L.-Y. (2008) A preliminary investigation of chlorine XANES in silicate glasses. *Geochem. Geophys. Geosys.* **9**(10), Q10003. https://doi.org/10.1029/2008GC002157

Ginstrup O. (1972) The redox system Platinum (0)/Platinum (II)/Platinum (IV) with chloro and bromo ligands. *Acta Chem. Scand.* **26,** 1527-1541.

Gammons C.H., Bloom M.S. and Yu Y. (1992) Experimental investigation of the hydrothermal geochemistry of platinum and palladium: I. Solubility of platinum and palladium sulfide minerals in NaCl/H_2SO_4 solutions at 300°C. *Geochim. Cosmochim. Acta* **56,** 3881-3894.

Gammons C.H. and Bloom M.S. (1993) Experimental investigation of the hydrothermal geochemistry of platinum and palladium: II. The solubility of PtS and PdS in aqueous sulfide solutions to 300°C. *Geochim. Cosmochim. Acta* **57,** 2451-2467.

Hanley J.J., Mungall J.E., Pettke T., Spooner E.T.C. and Bray C.J. (2008) Fluid and halide melt inclusions of magmatic origin in the ultramafic and lower banded series, Stillwater complex, Montana, USA. *J. Petrol.* **49,** 1133-1160.

Ho P.C. and Palmer D.A. (1997) Ion association in dilute aqueous potassium chloride and potassium hydroxide solutions to 600°C and 300 MPa determined by electrical conductance measurements. *Geochim. Cosmochim. Acta* **61,** 3027-3040.

Ho P.C., Palmer D.A. and Mesmer R.E. (1994) Electrical conductivity measurements of aqueous sodium chloride solutions to 600°C and 300 MPa. *J. Sol. Chem.* **23,** 997-1018.

Johnson J.W., Oelkers E.H. and Helgeson H.C. (1992) SUPCRT92: A software package for calculating the standard molal thermodynamic properties of minerals, gases, aqueous species, and reactions from 1 to 5000 bar and 0 to 1000°C. *Comp. Geosci.* 18, 899-947.

Kawaizumi F. (1992) Partial molar volumes of halogeno complexes of platinum and palladium in aqueous solutions and differences in volume between tetra- and hexa-coordinated forms. *J. Chem. Soc. Faraday Trans.* **88**(16), 2351-2353.

Kokh M.A., Akinfiev N.N., Pokrovski G.S., Salvi S. and Guillaume D. (2017) The role of carbon dioxide in the transport and fractionation of metals by geological fluids. *Geochim. Cosmochim. Acta* **197,** 433-466.

Korzhinsky M.A., Tkachenko S.I., Bulgakov R.F. and Shmulovich, K.I. (1996) Condensate compositions and native metals in sublimates of high-temperature gas streams of Kudryavy Volcano, Iturup Island, Kuril Islands. *Geochem. Int.* **36,** 1175–1182.

Mei Y., Etschmann B., Liu W., Sherman D.M., Barnes S.J., Fiorentini M.L., Seward T.M., Testemale D. and Brugger J. (2015) Palladium complexation in chloride- and bisulfide-rich fluids: Insights from *ab initio* molecular dynamics simulations and X-ray absorption spectroscopy. *Geochim. Cosmochim. Acta* **161,** 128-145.

Nikolaeva N.M. and Erenburg A.M. (1977) The effect of temperature on the standard potentials of the halogenide complexes of Pt^{II}. *Izvestiya Sibirskogo otdeleniya AN SSSR*, Ser. khimicheskih nauk, Vip. 4, 70-73.

Okamoto H. (1997) Ag-Pt (Silver-Platinum). *J. Phase Equilib.* **18,** 485.

Plotinskaya O.Y., Azovskova O.B., Abramov S.S., Groznova E.O., Novoselov K.A., Seltmann R. and Spratt J. (2018) Precious metals assemblages at the Mikheevskoe porphyry copper deposit (South Urals, Russia) as proxies of epithermal overprinting. *Ore Geol. Rev.* **94,** 239–260.

Pokrovski G.S. and Dubessy J. (2015) Stability and abundance of the trisulfur radical ion S_3^- in hydrothermal fluids. *Earth Plan. Sci. Let.* **411,** 298-309.

Ravel B. and Newville M. (2005) ATHENA, ARTEMIS, HEPHAESTUS: data analysis for X-ray absorption spectroscopy using IFEFFIT. *J. Synchr. Radiation* **12,** 537-541.

Sluzhenikin S.F. and Mokhov A.V. (2015) Gold and silver in PGE-Cu-Ni and PGE ores of the Norils'k deposits, Russia. *Miner. Deposita* **50,** 465-492.

Scholten L., Watenphul A., Beermann O., Testemale D., Ames D. and Schmidt C. (2018) Nickel and platinum in high-temperature H_2O + HCl fluids: Implications for hydrothermal mobilization. *Geochim. Cosmochim. Acta* **224,** 187–199.

Shmulovich K.I. and Churakov S.V. (1998) Natural fluid phases at high temperatures and low pressures. *J. Geochem. Expl.* **62,** 183-191.

Shmulovich K.I., Bukhtiyarov P.G. and Persikov E.S. (2016) Gold transport during magmatic degassing: model experiments. *Geochem. Int.* **54,** 979-988.

Shvarov Yu.V. (2008) HCh: New potentialities for the thermodynamic simulation of geochemical systems offered by Windows. *Geochem. Int.* **46,** 834-839.

Safonov O.G., Shiryaev A.A., Tyurnina A.V. and Huthwelker T. (2017) Structural features of quench products of melts in the chloride-carbonate-silicate systems revealed by vibrational and X-ray spectroscopy. *Petrology* **25**, 23-41.

Tagirov B.R., Zotov A.V. and Akinfiev N.N. (1997) Experimental study of dissociation of HCl from 350 to 500°C and from 500 to 2500 bars: Thermodynamic properties of $HCl_{(aq)}$. *Geochim. Cosmochim. Acta* **61,** 4267-4280.

Tagirov B.R., Baranova N.N., Zotov A.V., Akinfiev N.N., Polotnyanko N.A., Shikina N.D., Koroleva L.A., Shvarov Yu.V. and Bastrakov E.N. (2013) The speciation and transport of palladium in hydrothermal fluids: Experimental modeling and thermodynamic constraints. *Geochim. Cosmochim. Acta* **117,** 348-373.

Tagirov B.R., Baranova N.N. and Bychkova Y.V. (2015) Thermodynamic properties of platinum chloride complexes in aqueous solutions: derivation of consistent parameters from literature data and experiments on $Pt_{(cr)}$ solubility at 400 – 475 °C and 1 kbar. *Geochem. Int.* **53**(4), 327-340.

Tagirov B.R., Trigub A.L., Selivanov P.V. and Koroleva L.A. (2017) Composition and structure of Pt chloride complexes in hydrothermal solutions, according to X-ray absorption spectroscopy. *Russ. J. Phys. Chem. A* **91**(3), 543-548.

Tagirov B.R., Trigub A.L., Filimonova O.N., Kvashnina K.O., Nickolsky M.S., Lafuerza S. and Chareev D.A. (2019) Gold transport in hydrothermal chloride-bearing fluids: insights from in situ X-ray absorption spectroscopy and ab initio molecular dynamics. *ACS Earth and Space Chemistry* (DOI: 10.1021/acsearthspacechem.8b00103).

Trigub A.L., Tagirov B.R., Kvashnina K.O., Chareev D.A., Nickolsky M.S., Shiryaev A.A., Baranova N.N., Kovalchuk E.V. and Mokhov A.V. (2017a) X-ray spectroscopy study of the chemical state of "invisible" Au in synthetic minerals in the Fe-As-S system. *Am. Mineral.* **102,** 1057-1065.

Trigub A.L., Tagirov B.R., Kvashnina K.O., Lafuerza S., Filimonova O.N. and Nickolsky M.S. (2017b) Experimental determination of gold speciation in sulfide-rich hydrothermal fluids under a wide range of redox conditions. *Chem. Geol.* **471,** 52-64.

Yudovskaya M.A., Distler V.V., Chaplygin I.V., Trubkin N.V. and Gorbacheva S.A. (2006) Gaseous transport and deposition of gold in magmatic fluid: evidence from the active Kudryavy volcano, Kurile Islands. *Miner. Deposita* **40,** 828-848.

Wagner W. and Pruss A. (2002) The IAPWS formulation 1995 for the thermodynamic properties of ordinary water substance for general and scientific use. *J. Phys. Chem. Ref. Data* **31,** 387-535.

Webster J.D., Baker D.R. and Aiuppa A. (2018) Halogens in Mafic and Intermediate-Silica Content Magmas. In *The Role of Halogens in Terrestrial and Extraterrestrial Geochemical Processes* (eds. D.E. Harlov and L.Y Aranovich). Springer, pp. 307-430.

Xiong Y. and Wood S.A. (2000) Experimental quantification of hydrothermal solubility of platinum-group elements with special reference to porphyry copper environments. *Mineral. Petrol.* **68,** 1–28.

Zabinsky S.I., Rehr J.J., Ankudinov A., Albers, R. C. and Eller M.J. (1995) Multiple-scattering calculations of X-ray-absorption spectra. *Phys. Rev. B* **52,** 2995-3009.

Zhitova L.M., Kinnaird J.A., Gora M.P. and Shevko E.P. (2016) Magmatogene fluids of metal-bearing reefs in the Bushveld Complex, South Africa: based on research data on fluid inclusions in quartz. *Geol. Ore Deposits* **58**(1), 58-80.

Zotov A.V., Tagirov B.R., Koroleva L.A. and Volchenkova V.A. (2017) Experimental modeling of Au and Pt coupled transport by chloride hydrothermal fluids at 350-450°C and 500-1500 bar. *Geol. Ore Deposits* **59**(5), 421-429.

Zotov A.V., Kuzmin N.N., Reukov V.L. and Tagirov B.R. (2018) Stability of $AuCl_2^-$ from 25 to 1000 °C at pressures to 5000 bar and consequences for hydrothermal gold mobilization. *Minerals* **8**(7), 286.

Table 1. Compositions of experimental solutions and equilibrium concentrations of aqueous species (mol·(kg H_2O)$^{-1}$). Calculations were performed using thermodynamic data available in the literature (sources of thermodynamic data are listed in section 2.3) and calculated in the present study ($PtCl_4^{2-}$).

Capillary	cap119		cap120			cap125	
Solute concentr.	7.25*m* HCl/4.23*m* CsCl/ 0.56*m* H_2SO_4/0.12*m* Na_2SO_3					3.76*m* HCl/6.46*m* KCl/ 0.35*m* $K_2S_2O_8$	
d, g·cm^{-3}	0.86		1.01			0.96	
t, °C/ ***P***, bar	500 °C/ 1300 bar	575 °C/ 2100 bar	450 °C/ 3300 bar	525 °C/ 4500 bar	575 °C/ 5300 bar	450 C°/ 500 bar	525 °C/ 1300 bar
Calculated concentrations, mol·(kg H_2O)$^{-1}$							
H^+	1.60E-01	6.46E-02	1.36E+00	8.05E-01	5.39E-01	2.91E-02	2.59E-02
OH^-	1.36E-09	5.55E-09	1.09E-09	3.58E-09	7.76E-09	7.38E-09	8.71E-09
$H_2S°$	2.39E-08	1.79E-07	6.04E-08	1.44E-07	3.96E-07	2.34E-07	6.04E-10
HSO_3^-	1.44E-06	2.22E-06	2.15E-06	2.24E-06	2.22E-06	4.99E-06	3.45E-06
HSO_4^-	7.57E-02	2.67E-02	2.22E-01	7.11E-02	2.97E-02	2.07E-01	3.62E-01
HSO_5^-	5.83E-16	1.06E-14	1.77E-17	8.08E-16	4.78E-15	3.44E-17	4.49E-14
S_2^{--}	6.04E-27	2.44E-25	1.89E-26	6.13E-26	2.99E-25	1.99E-22	3.22E-28
$S_2O_3^{--}$	2.44E-16	3.71E-16	1.43E-15	4.96E-16	3.68E-16	1.46E-12	1.67E-16
$HS_2O_3^-$	1.79E-13	3.14E-13	3.94E-12	1.92E-12	1.62E-12	3.96E-12	1.70E-14
$H_2S_2O_3°$	1.69E-11	1.16E-11	3.22E-10	1.12E-10	6.95E-11	3.80E-10	3.46E-13
$S_2O_4^{--}$	2.15E-20	7.20E-20	4.39E-20	5.95E-20	7.82E-20	1.54E-17	6.53E-20
$HS_2O_4^-$	3.48E-17	1.16E-16	1.74E-16	2.88E-16	4.00E-16	1.38E-16	1.50E-17
$H_2S_2O_4°$	3.02E-15	3.93E-15	1.24E-14	1.51E-14	1.57E-14	1.67E-14	2.91E-16
$S_2O_5^{--}$	1.31E-17	1.64E-17	2.85E-17	2.09E-17	1.57E-17	5.02E-15	9.72E-17
$S_2O_6^{--}$	1.72E-15	1.04E-15	3.06E-15	1.59E-15	8.02E-16	2.90E-13	3.45E-14
$S_2O_8^{--}$	6.89E-22	2.10E-21	2.08E-23	1.77E-22	2.98E-22	2.53E-21	3.49E-19
S_3^{--}	4.01E-32	2.05E-30	9.39E-31	1.56E-30	6.81E-30	6.72E-27	9.34E-35
$S_3O_6^{--}$	1.19E-22	9.57E-23	2.05E-21	5.99E-22	2.84E-22	1.16E-19	1.04E-22
S_4^{--}	2.16E-37	1.41E-35	3.69E-35	3.20E-35	1.26E-34	1.95E-31	2.22E-41
$S_4O_6^{--}$	1.85E-19	9.64E-20	2.17E-17	1.52E-18	4.22E-19	2.09E-15	6.17E-21
SO_3^{--}	5.29E-15	8.80E-15	8.77E-15	9.14E-15	9.63E-15	7.06E-12	8.61E-14
SO_4^{--}	4.06E-06	1.07E-06	4.83E-06	9.49E-07	3.17E-07	8.19E-03	1.46E-04
HS^-	6.18E-15	7.20E-14	1.74E-14	4.21E-14	1.22E-13	2.52E-13	7.03E-16
Cl^-	6.45E-01	5.90E-01	1.89E+00	1.44E+00	1.27E+00	1.54E+00	8.20E-01
HCl°	5.84E+00	5.78E+00	5.12E+00	5.18E+00	5.32E+00	1.57E+00	2.01E+00
Na^+	1.13E-01	1.08E-01	1.25E-01	1.26E-01	1.26E-01	-	-
NaOH°	6.98E-11	1.86E-10	1.24E-11	2.70E-11	4.33E-11	-	-
NaCl°	1.22E-01	1.27E-01	1.12E-01	1.09E-01	1.09E-01	-	-
K^+						3.37E+00	2.51E+00
KOH°						2.06E-08	1.99E-08
KCl°						3.67E+00	4.57E+00
Cs^+	1.39E+00	1.49E+00	1.28E+00	1.53E+00	1.67E+00		
CsOH°	4.20E-10	1.31E-09	7.29E-11	2.10E-10	3.92E-10		
CsCl°	2.75E+00	2.65E+00	2.89E+00	2.61E+00	2.47E+00		
$H_2°$	4.87E-07	2.53E-06	9.26E-08	4.70E-07	1.46E-06	1.19E-06	2.98E-07
$O_2°$	7.26E-17	3.62E-15	1.25E-19	3.60E-17	6.20E-16	7.17E-19	4.58E-15
$SO_2°$	5.91E-01	6.39E-01	4.48E-01	5.96E-01	6.36E-01	4.73E-01	3.30E-01
$PtCl_4^{--}$	4.74E-01	5.22E-01	3.30E-01	4.78E-01	5.19E-01	8.17E-01	6.76E-01
$I^{(a)}$	2.1	2.2	3.1	2.9	2.9	4.2	3.2
pH	1.6	1.9	0.4	0.6	0.8	3.0	2.5
Eh	0.1	0.0	0.2	0.2	0.1	-0.1	0.0
$f(O_2)$, bar	-13.9	-12.0	-15.7	-13.2	-11.9	-16.5	-12.1

[a] ionic strength.

Table 2. Positions of the edge jump (e.j.), white line (WL), and the next to WL feature (B) of Pt L_3-edge XANES spectra (as determined by IFEFFIT program). Uncertainty of the energy values is ±0.5 eV.

Experimental system	Feature	Position, eV
H_2PtCl_6	e.j. WL B	11565.5 11568.0 11580.0
K_2PtCl_6	e.j. WL B	11565.5 11567.7 11579.7
K_2PtCl_4	e.j. WL B	11563.5 11566.0 11581.2
Cap 2160, melt ***t*** = 650 °C CsCl/NaCl/KCl 45.5at.%/30 at%/24.5 at%	e.j. WL B	11564.0 11566.5 11578.5
Cap 125 ***t*** = 450 °C, ***P*** = 500 bar 3.76*m* HCl/6.46*m* KCl + $K_2S_2O_8$	e.j. WL B	11563.5 11566.5 11578.5
Cap125 ***t*** = 525 °C, ***P*** = 1300 bar	e.j. WL B	11563.5 11566.5 11578.5
Cap 120 ***t*** = 450 °C, ***P*** = 3300 bar 7.25*m* HCl/4.23*m* CsCl + H_2SO_4/Na_2SO_3	e.j. WL B	11563.5 11566.5 11578.5
Cap 120 ***t*** = 525 °C, ***P*** = 4500 bar	e.j. WL B	11563.5 11566.5 11578.0
Cap 120 ***t*** = 575 °C, ***P*** = 5300 bar	e.j. WL B	11563.5 11566.5 11578.5
Cap 119 ***t*** = 500 °C, ***P*** = 1300 bar 7.25*m* HCl/4.23*m* CsCl + H_2SO_4/Na_2SO_3	e.j. WL B	11563.5 11566.5 11578.5
Cap 119 ***t*** = 575 °C, ***P*** = 2100 bar	e.j. WL B	11563.5 11566.5 11578.5

Table 3. Results of EXAFS spectra fitting (ARTEMIS program, $S_0^2 \sim 0.80$). Experimental spectra fits were performed in *k*-space. *Left* – Model with the second coordination sphere cation. *Right* – Model without the second coordination sphere cation.

Model with the second coordination sphere cation						Model without the second coordination sphere cation					
Atom	EXAFS					Atom	EXAFS				
	N	*R*, Å	σ^2, Å^{-2}	Fit quality			*N*	*R*, Å	σ^2, Å^{-2}	Fit quality	
				E^0, eV	Red chi ^{2} (R-factor)					E^0, eV	Red chi ^{2} (R-factor)
CsCl/NaCl/KCl melt											
Cap 2160 (*k*-range 3 – 13), ***t*** = 650 °C.											
Cl **Cs** **MS**	3.89±0.50 1 3.89	2.30±0.01 3.72±0.06 4.59±0.06	0.005±0.001 0.006±0.006 0.017±0.009	6.3±1.5	20914.4 (0.054)	**Cl** **MS**	3.85±0.47 3.85	2.30±0.01 4.61±0.06	0.005±0.001 0.018±0.009	6.2±1.4	19097.3 (0.057)
HCl/CsCl aqueous fluid (7.25*m* HCl/4.23*m* CsCl/0.56*m* H_2SO_4/0.12*m* Na_2SO_3)											
Cap 119 (*k*-range 3 – 11), ***t*** = 500 °C, ***P*** = 1300 bar.											
Cl **Cs** **MS**	4.01±0.62 1 4.01	2.32±0.01 3.68±0.11 4.65±0.07	0.004±0.002 0.009±0.014 0.016±0.011	9.5±1.7	8735.7 (0.060)	**Cl** **MS**	4.01±0.58 4.01	2.32±0.01 4.65±0.05	0.004±0.002 0.014±0.008	9.3±1.5	7806.7 (0.063)
Cap 119 (*k*-range 3 – 12), ***t*** = 575 °C, ***P*** = 2100 bar.											
Cl **Cs** **MS**	3.95±0.76 1 3.95	2.32±0.02 3.65±0.14 4.61±0.09	0.005±0.002 0.010±0.017 0.019±0.015	8.8±2.1	7201.6 (0.091)	**Cl** **MS**	3.93±0.71 3.93	2.31±0.01 4.62±0.07	0.005±0.002 0.016±0.011	8.6±1.9	6393.2 (0.095)

Table 3 – continued

Cap 120 7.25*m* HCl/4.23*m* CsCl + H_2SO_4/Na_2SO_3 (*k*-range 3 – 12), ***t*** = 450 °C, ***P*** = 3300 bar.											
Cl **Cs** **MS**	3.90±0.68 1 3.90	2.31±0.01 3.51±0.08 4.64±0.08	0.004±0.002 0.007±0.009 0.015±0.012	8.8±1.9	7031.6 (0.080)	**Cl** **MS**	3.94±0.64 3.94	2.31±0.01 4.63±0.06	0.004±0.002 0.013±0.010	8.7±1.7	6084.5 (0.083)
Cap 120 (*k*-range 3 – 12), ***t*** = 525 °C, ***P*** = 4500 bar.											
Cl **Cs** **MS**	3.74±0.57 1 3.74	2.31±0.01 4.12±0.05 4.67±0.09	0.003±0.001 0.002±0.004 0.020±0.015	8.3±1.7	4604.5 (0.063)	**Cl** **MS**	3.73±0.55 3.73	2.30±0.01 4.63±0.06	0.003±0.001 0.014±0.009	8.1±1.6	4268.5 (0.069)
Cap 120 (*k*-range 3 – 11.5), ***t*** = 575 °C, ***P*** = 5300 bar.											
Cl **Cs** **MS**	3.74±0.65 1 3.74	2.31±0.01 3.70±0.06 4.61±0.08	0.004±0.002 0.005±0.006 0.019±0.015	8.4±1.9	8051.9 (0.070)	**Cl** **MS**	3.68±0.62 3.68	2.31±0.01 4.63±0.07	0.004±0.002 0.016±0.012	8.2±1.8	7644.7 (0.079)
HCl/KCl aqueous fluid (3.76*m* HCl/6.46*m* KCl/0.35*m* $K_2S_2O_8$)											
Cap 125 (*k*-range 3 – 11), ***t*** = 450 °C, ***P*** = 500 bar.											
Cl **K** **MS**	3.64±0.46 1 3.64	2.31±0.01 3.44±0.13 4.62±0.04	0.003±0.001 0.016±0.021 0.006±0.006	8.7±1.3	5157.5 (0.033)	**Cl** **MS**	3.64±0.44 3.64	2.31±0.01 4.63±0.04	0.003±0.001 0.006±0.005	8.5±1.2	4650.2 (0.036)
Cap 125 (*k*-range 3 – 11.5), ***t*** = 525 °C, ***P*** = 1300 bar.											
Cl **K** **MS**	3.83±0.67 1 3.83	2.30±0.01 3.85±0.07 4.63±0.06	0.005±0.002 0.003±0.009 0.012±0.009	7.4±1.8	16124.9 (0.071)	**Cl** **MS**	3.85±0.60 3.85	2.30±0.01 4.62±0.06	0.005±0.002 0.013±0.008	7.7±1.7	12965.5 (0.069)
Multiple scattering MS = Pt-Cl1-Pt-Cl2.											

Table 4. The Pt solubility constants, $K°_s(PtCl_4^{2-})$, of the reaction $Pt_{(cr)}$ + 2 $HCl°_{(aq)}$ + 2 Cl^- = $PtCl_4^{2-}$ + $H_{2(aq)}$ fitted to the density model equation.

t, C	*P*, bar	log $K°_s$	Source
25	1	-26.50±0.24	[a]
25	1000	-26.71	[b]
50	1	-24.29±0.12	[a]
100	$P_{sat.}$	-20.86±0.05	[a]
150	$P_{sat.}$	-18.41±0.07	[a]
350	1000	-12.39±0.3	[c]
450	500	-9.53±0.16	[c]
450	1000	-9.42±0.27	[c]

[a] adopted from Tagirov et al. (2015), data are based on the experimental potentiometric results of Nikolaeva and Erenburg (1977) and Ginstrup (1972);
[b] calculated using the value of $V°(PtCl_4^{2-})$ from Kawaizumi (1992) and the value of log $K°_s$ for 25°C, 1 bar from this table;
[c] calculated using data of Zotov et al. (2017) and Zotov et al. (2018) as described in section 3.3.

Table 5. The Pt solubility constant, $K_s°(PtCl_4^{2-})$, of the reaction $Pt_{(cr)}$ +2 $HCl°_{(aq)}$ +2 Cl^- = $PtCl_4^{2-}$ + $H_2°_{(aq)}$ as a function of temperature and pressure. Calculations were performed using Eq. (8) obtained in the present study.

t, °C	*P*, bar					
	$P_{sat.}$	500	1000	1500	2000	5000
25	-26.54	-26.52	-26.51	-26.49	-26.48	-26.42
100	-21.02	-21.01	-21.01	-21.01	-21.00	-20.99
200	-16.31	-16.33	-16.34	-16.34	-16.35	-16.38
250	-14.58	-14.61	-14.63	-14.65	-14.67	-14.72
300	-13.10	-13.16	-13.20	-13.23	-13.25	-13.34
350	-11.72	-11.88	-11.96	-12.01	-12.04	-12.16
400		-10.69	-10.86	-10.94	-10.99	-11.15
450		-9.41	-9.86	-9.98	-10.06	-10.26
500		-8.09	-8.91	-9.11	-9.22	-9.48
550			-8.00	-8.30	-8.45	-8.78
600			-7.16	-7.55	-7.74	-8.15
650			-6.38	-6.85	-7.09	-7.58
700			-5.69	-6.21	-6.48	-7.05
750				-5.61	-5.92	-6.57
800				-5.06	-5.40	-6.13
850				-4.56	-4.92	-5.72
900				-4.09	-4.47	-5.33
950				-3.66	-4.05	-4.97
1000				-3.26	-3.67	-4.64

Table 6. Experimental data on the solubility of Pt in coexisting vapor-brine-rhyolite melt system at 800 °C, 1000 and 1400 bar (Simon and Pettke, 2009), and results of thermodynamic modeling of the experiment.

Calculation	Type of inclusion	$P_{eff.}$[a], bar	$d^*_{H_2O}$[b], g·cm^{-3}	NaCl concentration, wt%		HCl concentration, mol·(kg H_2O)$^{-1}$	Pt concentration, mol·(kg H_2O)$^{-1}$		
				Experiment[c]	Calculated[d]		Experiment	Calculated $PtCl_4^{2-}$[e]	Calculated $PtCl_2°_{(aq)}$
***P* = 1400 bar, Ag-AgCl buffer of HCl activity**									
A	Brine	3279	0.575	~ 43	50.1	2.37[f]	$1.7·10^{-4}$	$2.9·10^{-4}$	$4.8·10^{-5}$
B	Vapor	1632	0.365	~ 9	8.5	3.13[f]	$5.1·10^{-6}$	$1.1·10^{-5}$	$3.3·10^{-5}$
***P* = 1000 bar, without buffer of HCl activity**									
Concentrations of HCl in brine and vapor phases are adopted from Simon and Pettke (2009)									
C	Brine	3189	0.567	~ 63	66.4	2.8[g]	$5.0·10^{-5}$	$8.1·10^{-3}$	-
D	Vapor	1034	0.239	~ 2	2.0	0.5[g]	$1.9·10^{-6}$	$4.6·10^{-10}$	-
Concentration of HCl in brine is calculated in the present study using the experimental Pt solubility data from Simon and Pettke (2009) and log $K_s°(PtCl_4^{2-})$ *from the present study (Eq.8)*									
E	Brine	3189	0.567	~ 63	66.4	0.22[h]	$5.0·10^{-5}$	$5.0·10^{-5}$	$3.8·10^{-7}$
F	Vapor	1034	0.239	~ 2	2.0	0.83[i]	$1.9·10^{-6}$	$1.3·10^{-9}$	$1.9·10^{-6}$[j]

[a] effective pressure, see section 2.3 for calculation details; [b] pure water density which corresponds to $P_{eff.}$, this value was used to calculate the Pt solubility reaction constant with Eq. 8; [c] wt% NaCl eq.; [d] calculated using Driesner and Heinrich (2007) EoS for H_2O-NaCl binary system; [e] calculated using thermodynamic properties of $PtCl_4^{2-}$ obtained in the present study; [f] calculated for equilibrium with the Ag-AgCl buffer assuming a(Ag) = X(Ag) =0.7 in Pt-Ag alloy; [g] – Simon and Pettke (2009) estimation; [h] estimated using experimental Pt concentration determined in brine given in the next column; [i] calculated using our estimation of the concentration of HCl in brine (see [g]) and thermodynamic data for $HCl°_{(aq)}$; [j] calculated using $g°(PtCl_2°_{(aq)})$ = -298.7 kJ·mol^{-1} at these T-$P_{eff.}$ parameters (800 °C, 1034 bar).

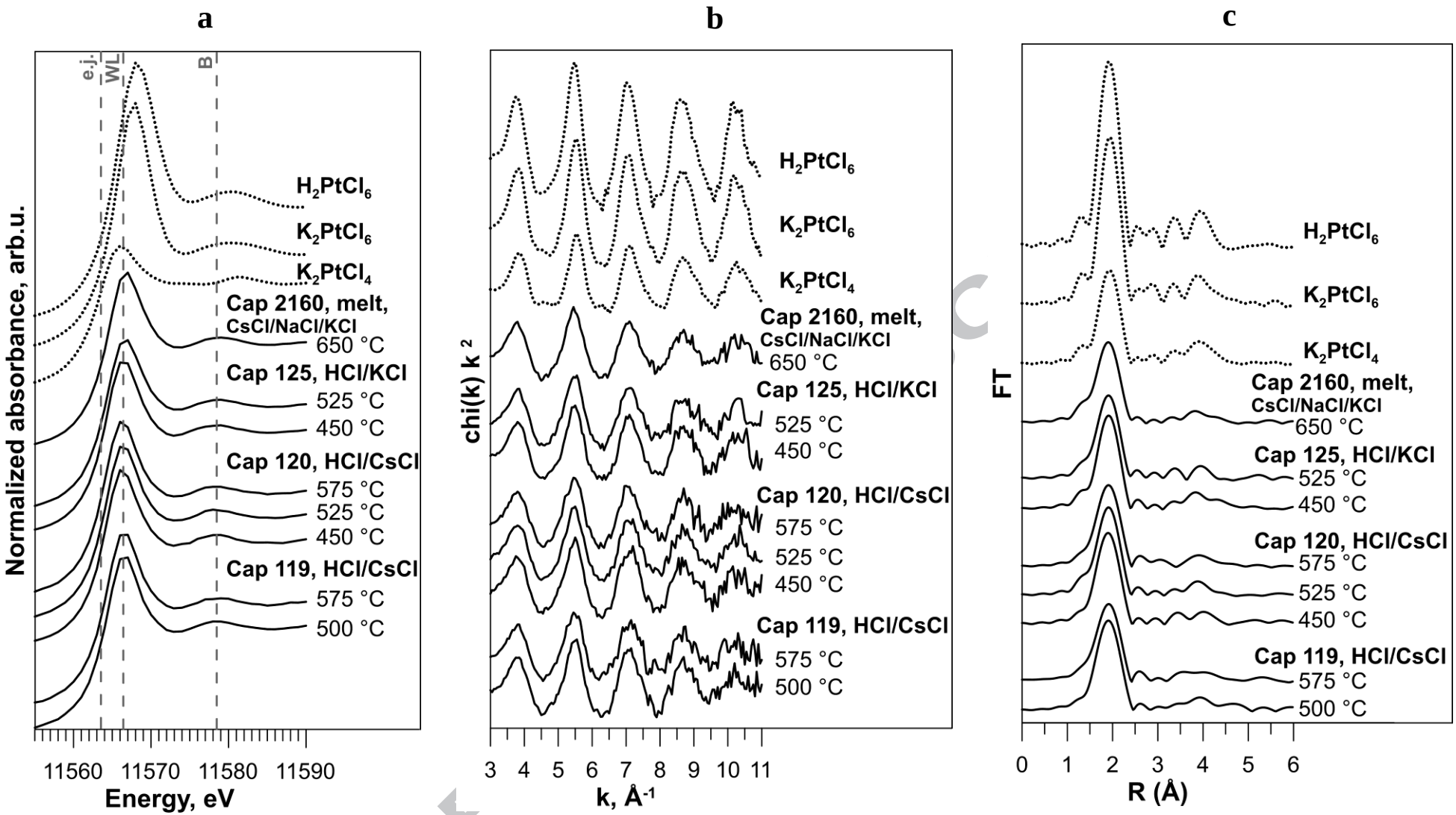

Fig. 1

Cap 2160, melt (*k*-range 3 – 13), ***t*** = 650 °C.

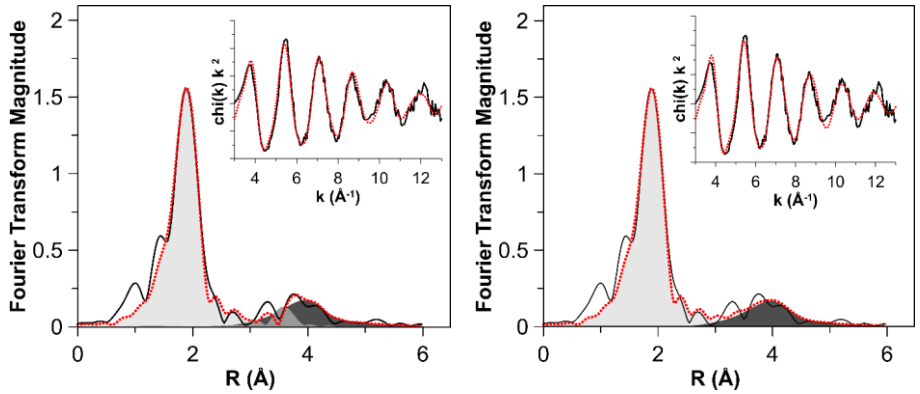

Cap 120 (*k*-range 3 – 12), ***t*** = 450 °C, ***P*** = 3300 bar.

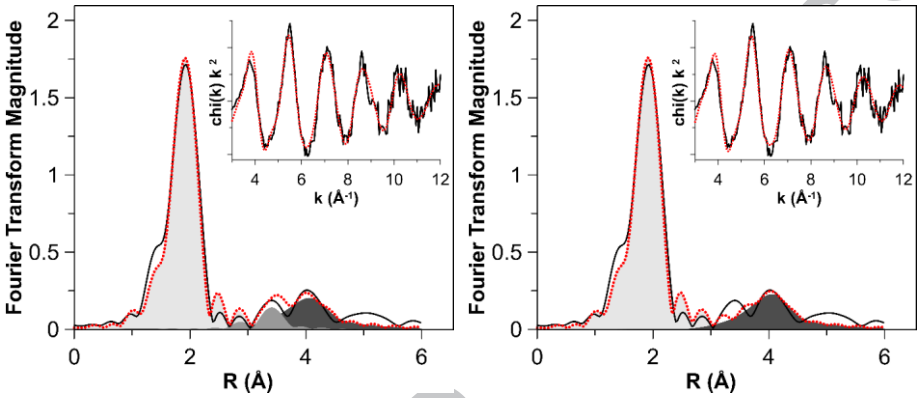

Cap 120 (*k*-range 3 – 12), ***t*** = 525 °C, ***P*** = 4500 bar.

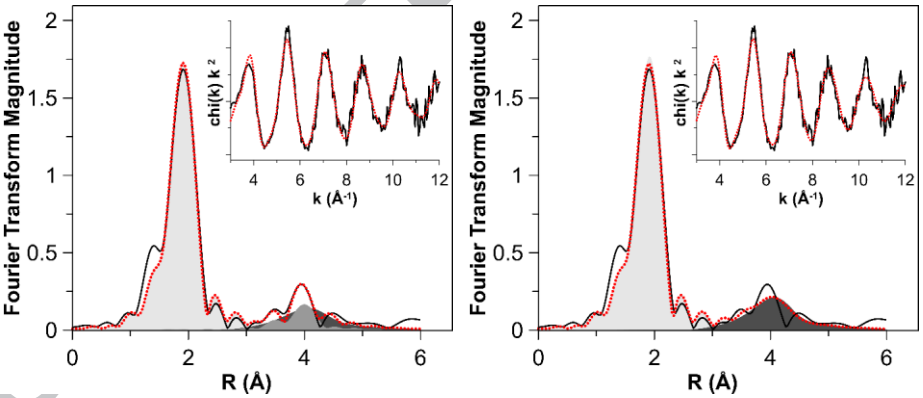

Cap 120 (*k*-range 3 – 11.5), ***t*** = 575 °C, ***P*** = 5300 bar.

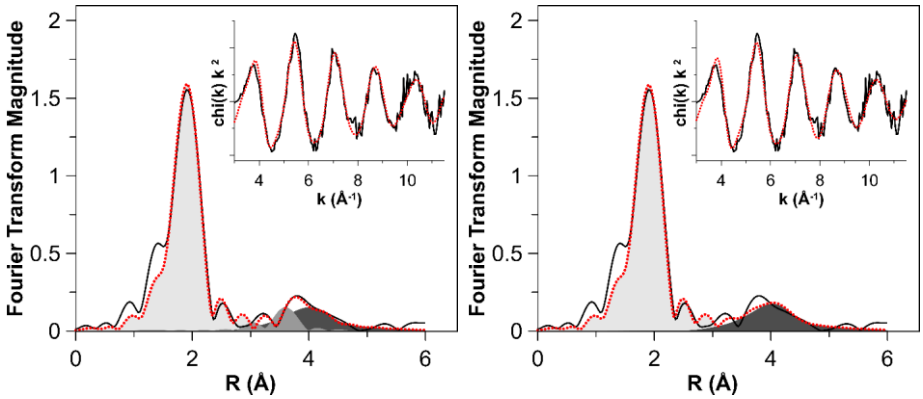

Fig. 2

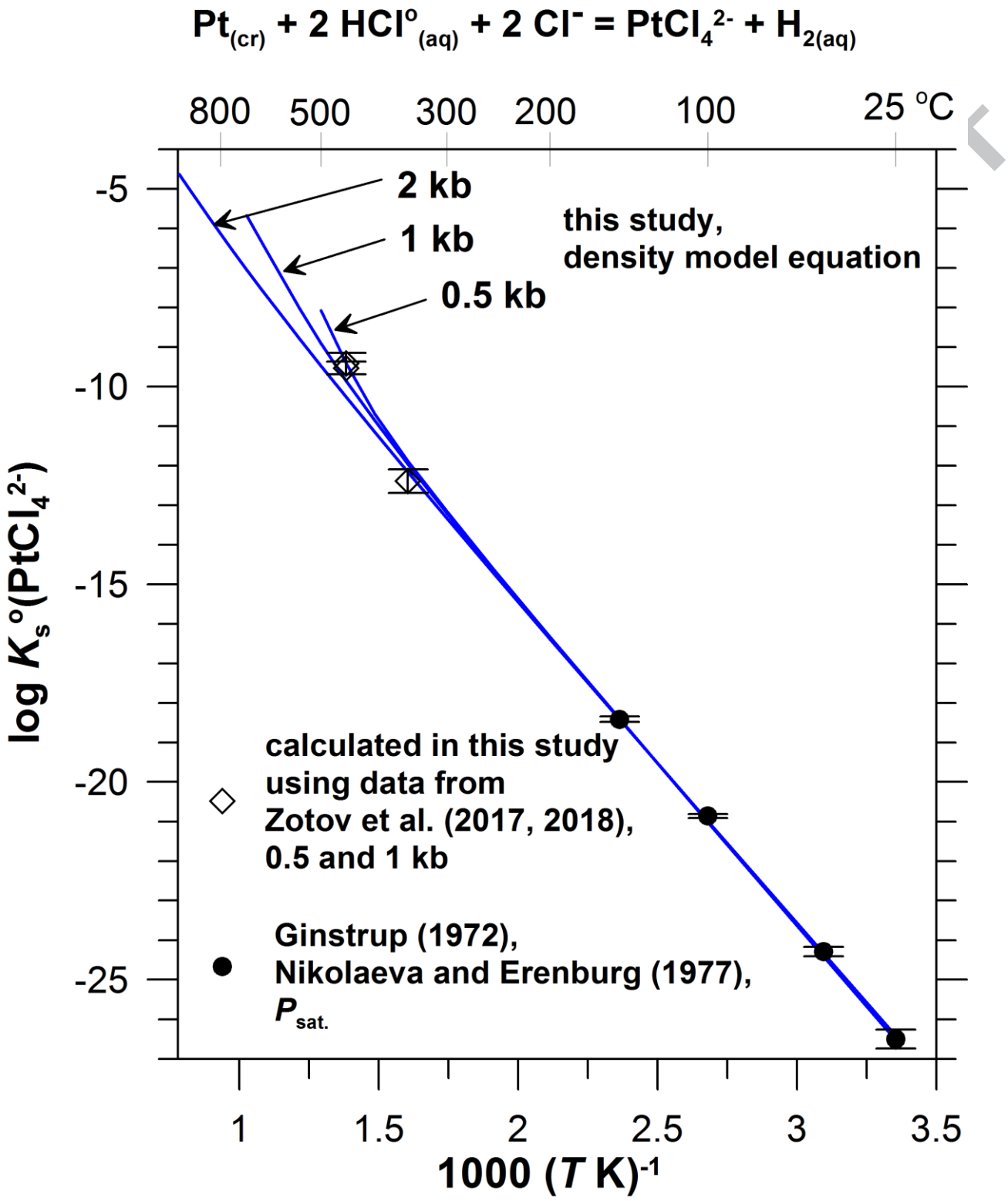

Fig. 3

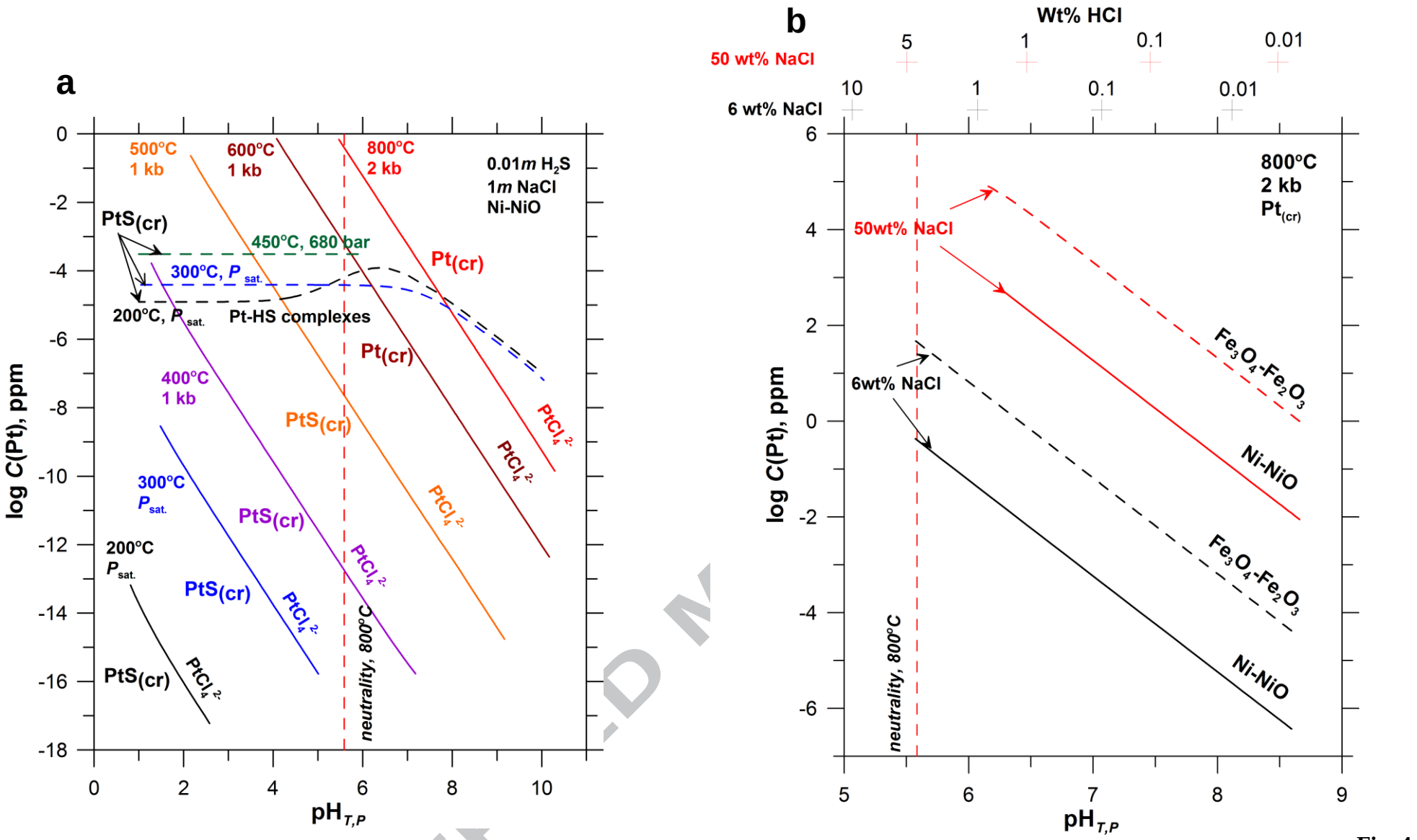

Fig. 4

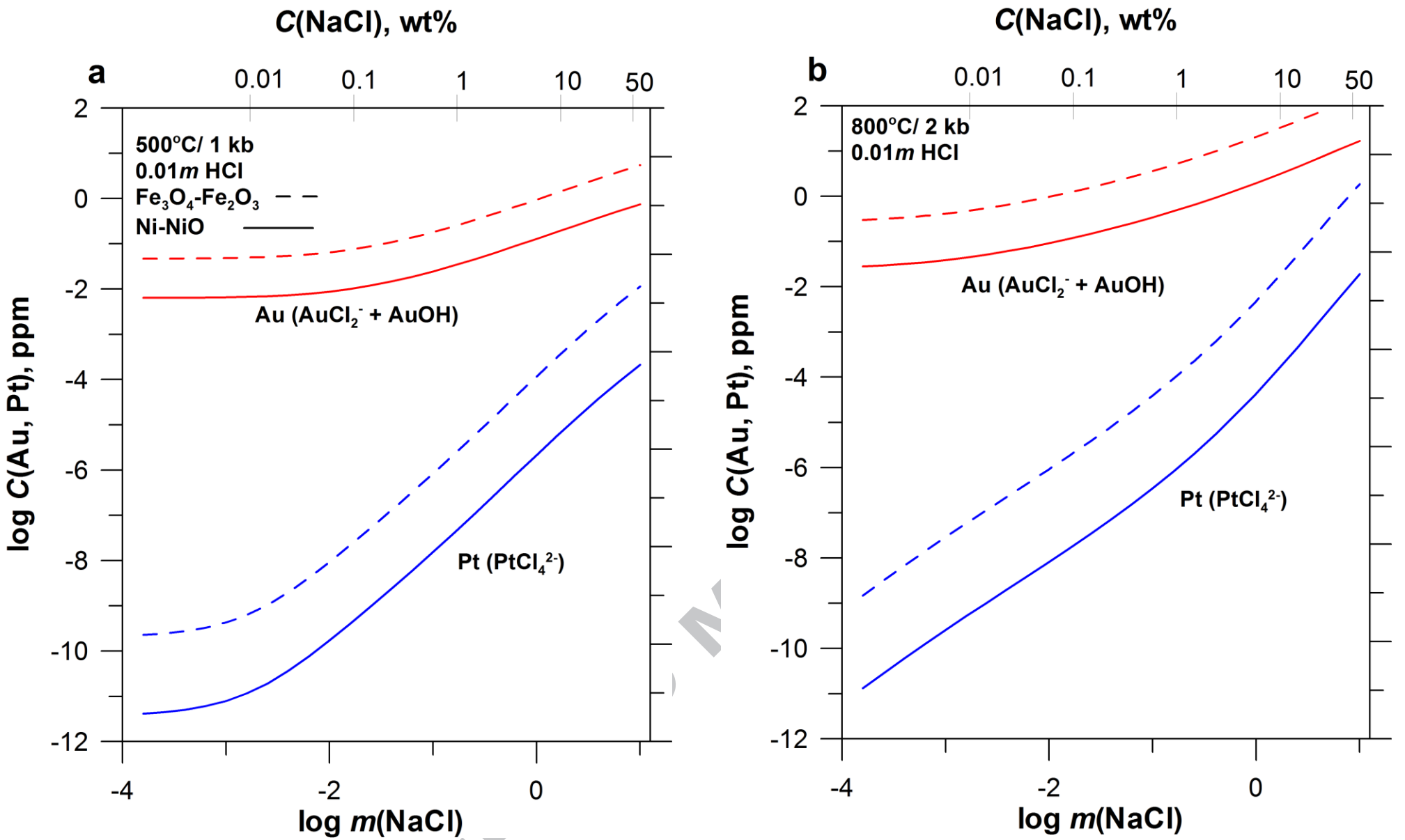

Fig. 5

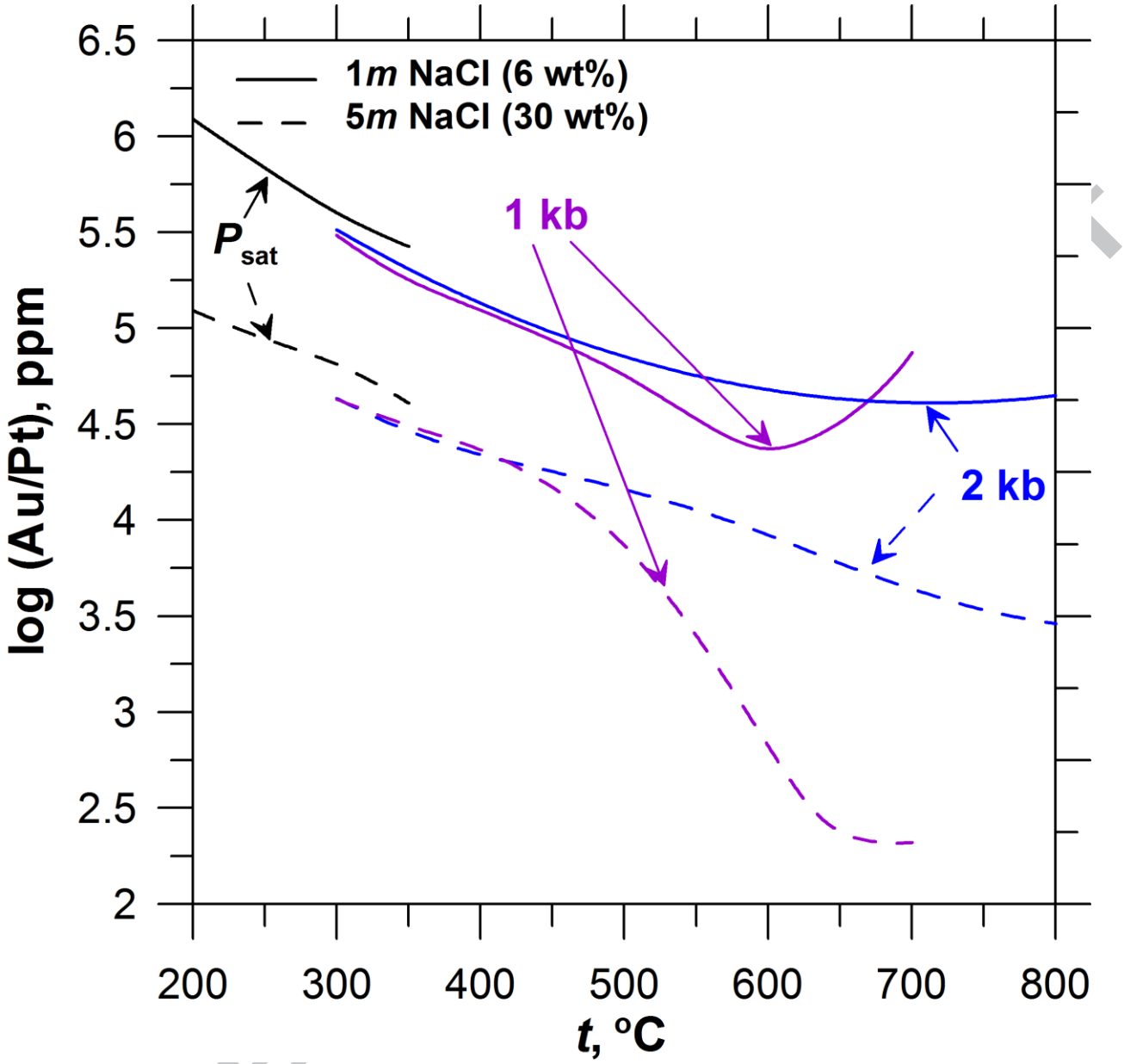

Fig. 6